HIGH TEMPERATURE AGING STUDY ON LONG-TERM AGED ALLOY 617 AND ALLOY 230

BY

YANG ZHAO

THESIS

Submitted in partial fulfillment of requirements
for the degree of Master of Science in Nuclear, Plasma and Radiological Engineering
in the Graduate College of the
University of Illinois at Urbana-Champaign, 2012

Urbana, Illinois

Master's Committee:

Professor James F. Stubbins, Adviser

Associate Professor Brent J. Heuser

Abstract

Alloy 617 and Alloy 230 are lead structural materials for next generation nuclear power plant (NGNP). Both alloys possess good corrosion resistance and exceptional high-temperature strength. In order to gain a better understanding of the high-temperature degradation process of these materials, long-term (up to 10000 hours) aging experiments have been carried out to investigate the microstructural evolution and mechanical property development for both alloys.

In the present study, focus is placed on the alloys aged for 10000 hours. Tensile and hardness tests were conducted. EDS coupled SEM and EBSD techniques were applied to reveal microstuctural characters of both alloys. Tensile tests were performed at strain rate of 10^{-3}/s and in temperature range from room temperature to 1000^{o}C. The Portevin-LeChatelier effect was observed and strain-rate sensitivities were studied. The tensile tests at room temperature show that both alloys softened significantly after aging at 1000ºC for 10000 hours, and the strength of both alloys was improved when aging at 900ºC. However, both long-term aged alloys, especially Alloy 230, exhibit high strength at high temperature. Carbide particle (mainly $M_{23}C_6$ and M_6C) growth is known to be a dominant microstructual feature during long-term aging at elevated temperatures. The evolution of the carbide structure is also the major contributor to dislocation pile-up enhancement, dynamic recrystallization (DRX) area fraction increase and fracture mechanisms change, which in turn influence mechanical properties.

Acknowledgements

Support and help from many people make it possible for completion of this thesis work.

I would like to express my appreciation to my advisor and department head, Dr. James F. Stubbins, for his guidance and support throughout the Master's program. I would like to thank Dr. Brent J. Heuser for his kindness and patience in reviewing this thesis as the second reader.

I would like to give my special thank to Dr. Kun Mo at China Nuclear Power Technology Research Institute for long-term aging experiment and generously sharing his ideas about microstructual analysis.

I am grateful to Dr. Hsiao-Ming Tung and Dr. Xiang Chen at University of Illinois, for their contribution and revelatory discussion on specimen preparation and instruments introduction.

I wish to thank Senior Research Scientist, Gavin Horn, at Mechanical Engineering Department in University of Illinois, for his kindness assistance on tensile instruments and maintenance. I would like to thank Center for Microanalsis of Materials in Frederick Seitz Material Research Laboratory for allowing me to use state-of-the-art scanning electron microscopy.

I also would like to express my appreciation to my family and my girl friend. Without their kind help and emotional support, the completion of the thesis work would be impossible.

The work was supported by US Department of Energy under grants DE-FC07-07ID14819 and DOE NEUP 09-516. Test materials were provided by Haynes International, Inc.

Table of Contents

Chapter 1 – Introduction

1.1 Generation IV International Forum (GIF)

Growing word's population and increasing striving for better quality of life pose demand for energy supplies that are clean and highly efficient. Now they are in total over 440 commercial nuclear power plant in 30 countries that contribute 14% of the world's electricity, which is 377,000 MWe of total capacity [1]. The importance of reducing greenhouse gas emission is recognized, which drives the nuclear energy growth around the world. However, several challenges for future utilize large-scale nuclear energy still exist: sustainable use of nuclear energy fuel sources, proper nuclear waste disposal, and reduce the risk of nuclear weapons proliferation [2].

To develop nuclear energy and deal with these challenges, thirteen members (Argentina, Brazil, Canada, China, Euratom, France, Japan, Korea, Russia, South Africa, Switzerland, United Kingdom and United States) joined together to form Generation IV International Forum (GIF) [3]. Six nuclear systems were selected for future Generation IV reactor concepts: Gas-Cooled Fast Reactor System (GFR), Lead-Cooled Fast Reactor System (LFR), Molten Salt Reactor (MSR), Sodium-Cooled Fast Reactor System (SFR), Supercritical-Water-Cooled Reactor System (SCWR) and Very-High-Temperature Reactor System (VHTR). These six nuclear systems all have significant different features and technical requirements. The Gas-Cooled Fast Reactor (GFR) system features a fast-neutron spectrum and closed fuel cycle for uranium and actinides conversion. The reference GIF reactor is 600-MWth, helium-cooled system with 850^{o}C output

temperature. The Lead-Cooled Faster Reactor (LFR) system features a fast-neutron spectrum and closed fuel cycle. Several options are proposed for LFR design: battery system of 50-150 MWe, modular type system of 300-400 MWe, and a plant design rated at 1200 MWe.

Table 1.1 Overview of Generation IV reactor systems [2]

System	Neutron Spectrum	Coolant	Temperature (^{o}C)	Fuel Cycle	Output power level (MWe)
VHTR	Thermal	Helium	900-1000*	Open	250-300
SFR	Fast	Sodium	550	Closed	30-150, 300-1500, 1000-2000
SCWR	Thermal/Fast	Water	510-625	Open/Closed	300-700, 1000-1500
GFR	Fast	Helium	850	Closed	1200
LFR	Fast	Lead	480-800	Closed	20-180, 300-1200, 600-1000
MSR	Fast/Thermal	Fluoride Salts	700-800	Closed	1000

* Temperature range was changed to 760^{o}C~950^{o}C

Molten Salt Reactor (MSR) system features an epithermal to thermal neutron spectrum and a closed fuel cycle for utilizing plutonium and minor actinides. Sodium-Cooled Faster Reactor (SFR) System applies a fast-neutron spectrum and a closed fuel cycle. Two designs are proposed: intermediate size (150 to 500 MWe) reactor that utilizes uranium-plutonium-minor-actinide-zirconium metal alloy fuel, and medium to large (500

to 1500 MWe) reactor with mixed uranium-plutonium oxide fuel. Supercritical-Water-Cooled Reactor (SCWR) system applies two different fuel cycles: open cycle coupled with thermal neutron spectrum and closed cycle with fast neutron spectrum. The reference SCWR operates above the thermodynamic critical point of water (22.1 MPa, 374^{o}C), which has a 1700-MWe power level, output temperature of 550^{o}C and operating pressure of 25 MPa, and thermal efficiency approximately 44%.

The Very High Temperature Reactor (VHTR) system uses a thermal neutron spectrum and a once-through uranium cycle. This system is developed for high temperature application, especially for highly efficient electricity generation (~90% output power) and hydrogen production (~10% output power) [4]. A detailed description of the VHTR will be discussed in the next session. Table 1.1 summarizes the major parameters of Generation IV systems.

1.2 Very High Temperature Reactor (VHTR)

The Very High Temperature Reactor (VHTR) is an appealing GEN-IV system due to its potential for very efficient energy generation. Development of this advanced nuclear reactor concept is under consideration in US and China. The VHTR is a graphite-moderated, helium-cooled reactor with dual capacities of high-efficiency electricity production and hydrogen generation. The Very High Temperature Reactor was developed to produce massive amounts of hydrogen in order to satisfy the demands for alternatives to fossil fuels because of global warming concerns. The intended output temperature of helium is up to 950^{o}C [5], which enables the hydrogen production by the thermochemical

sulfur-iodine cycle. Fig. 1.1 shows the VHTR design coupled with hydrogen production plant.

High temperature alloys must be designed and developed to take advantage of benefits of the VHTR. The operating atmosphere in the reactor system is a great challenge for structural components, especially the intermediate heat exchanger (IHX). These components are required to withstand high temperatures, high pressures (up to 7 MPa) and an aggressive atmosphere for a design life of 60 years [5]. Fig 1.2 shows the schematic of IHX and configurations parameters of VHTR system.

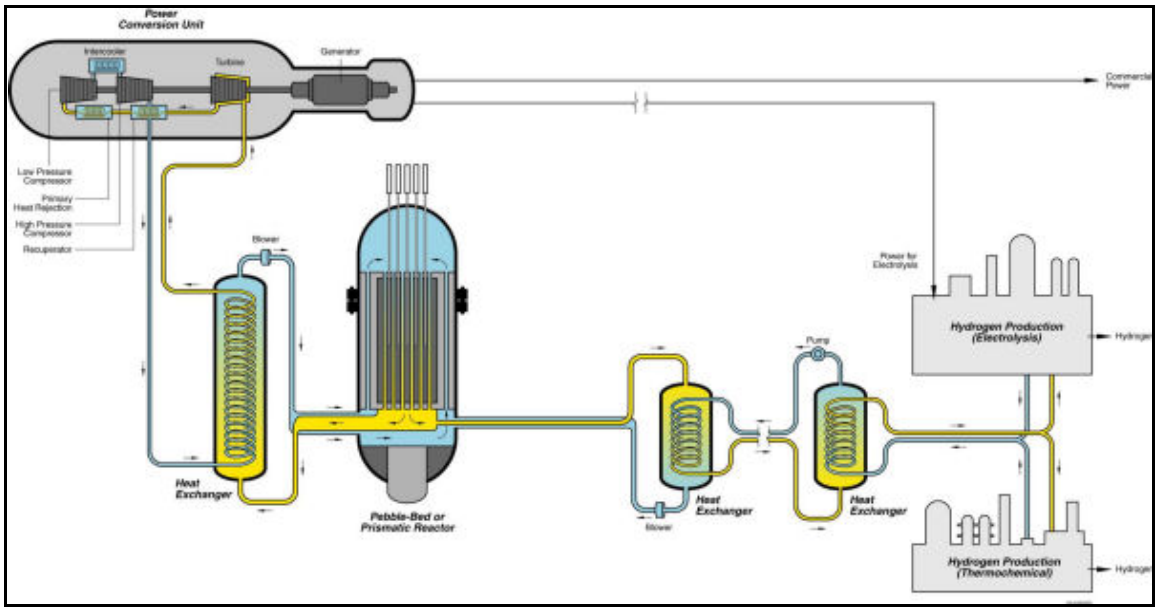

Fig 1.1 Schematic VHTR Design [2]

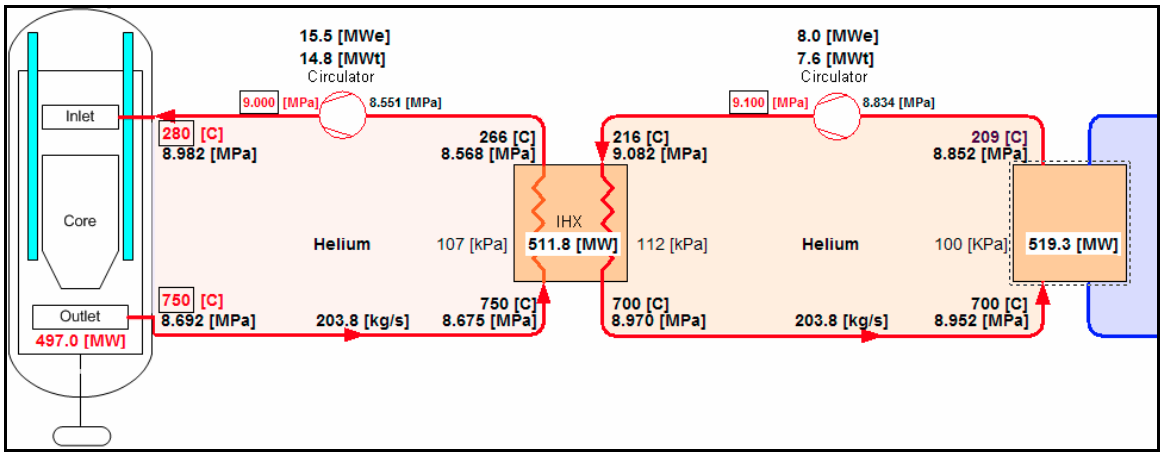

Fig 1.2 NGNP configuration as proposed by Westinghouse [6]

1.3 Alloy 617 and Alloy 230

INCONEL® Alloy 617 (UNS N06617/W.Nr. 2.4663a) is a solid-solution strengthened, nickel-chromium-cobalt-molybdenum alloy with an exceptional combination of high-temperature strength and oxidation resistance [7]. Alloy 617 was chosen as one of the top priority candidate materials for applications in the temperature range from 760^{o}C to 1,000^{o}C. In 1970's, a large amount of data on Alloy 617 have been generated for a variety of applications: gas turbines, chemical manufacture, and power generation structures. In the mid-1980s, a draft code case was developed for Alloy 617 applications for the High-Temperature Gas-Cooled Reactor, which covered temperature up to 950^{o}C. Unfortunately, the code case was dropped due to the termination of the HTGR program. Since then, more applicable data has been generated in Germany since then. Because the original VHTR application design required materials that would withstand temperatures as high as 1000^{o}C and toleration of the working conditions for more than 60 years, Alloy 617 has now regained a great deal of attention [8].

HAYNES® 230 Alloy is a solid-solution strengthened nickel-chromium-tungsten alloy, and displays good elevated temperature strength and environment resistance. HAYNES 230 Alloy can be utilized at temperatures as high as 2100°F (1150°C) for continuous service [9]. It is a relatively newly developed alloy that is applicable for gas turbine and heat exchanger application and is also considered to be a candidate material for the IHX of the VHTR. Compared to Alloy 617, a sufficient amount of experimental data on material performance for Alloy 230 is not available.

1.4 Literature Review

The Very high Temperature Reactor (VHTR) system is an extension of the previous High Temperature Gas-Cooled Reactor (HTGR). One of the popular designs of the HTGR family is Gas-Turbine-Modular Helium Reactor (GT-MHR), which is being developed by Russia for disposition of weapons-grade Plutonium and initially comes from the U.S. DOE/General Atomics (GA) concept [10]. Table 1.2 summarized the comparison of the VHTR and the GT-MHR.

The timeline of Very High Temperature Reactor development originally started from the late 1970's. Arbeitsgemeinschaft Versuchsreaktor (AVR) was the first experimental pebble bed reactor. Based on this design, a commercial reference pebble bed was developed, the Thorium High-Temperature Reactor (THTR). The only reactor that is still in operation in High Temperature Gas-Cooled Reactor family is the High-Temperature Test Reactor (HTTR) in Japan [11]. Table 1.3 shows the design characteristics of VHTRs that have been built and operated.

Table 1.2 Partial design parameters of VHTR and GT-MHR [10]

Conditions and Feature	GT-MHR	VHTR
Power Output (MW(t))	600	600
Coolant	Helium	Helium
Pressure (MPa)	7.12	7.12
Moderator	Graphite	Graphite
Plant Design Life	60	60
Core outlet temperature (^{o}C)	850	1000*
IHX	NA	Compact heat exchanger

* Temperature range was changed to 760^{o}C~950^{o}C

Table 1.3 Design parameters of VHTR that have been operated [11]

	Dragon	AVR	Peach Bottom	Ft. St. Vrain	THTR-300	HTTR
Country of Origin	OECD/Britain	Germany	U.S.	U.S.	Germany	Japan
Thermal Power (MWt)	21.5	46	115	842	750	30
Maximum Core Outlet Temp (^{o}C)	750	950	725	775	750	950
Reactor Type	Sleeve	Pebble	Sleeve	Block	Pebble	Prism
Date of Operation	1964-1975	1966	1967	1979-1989	1985	1997

Similar to the GT-MHR, the VHTR has more severe high-temperature environments for materials. Creep, fatigue, corrosion and aging damage of structural materials are inevitable. Since the objective of the thesis is the long-term aging research on both alloys, the literature review will mainly focus on aging effects. Mankins et al. [12] published a paper on aging effects of Alloy 617 in the temperature range of 649-1093^{o}C with aging time up to 1000 h. The author evaluated microstructrual properties of Alloy 617 with creep specimens because of the close approximation of long-term exposure to heat in the real operation conditions. The study showed that the major precipitates presented in the alloy were $M_{23}C_6$ after long-term aging. Two other carbide precipitate phases, MC and M_6C, were not identified. The gamma prime phase Ni_3Al was found to be stable after specimen exposure to 760^{o}C, providing some strengthening in the temperature range from 649 to 760^{o}C. At higher temperatures where gamma prime disolves, discrete $M_{23}C_6$ precipitates strengthening is the major strengthening mechanism. Kimball et al. [13] extended the aging time to 8000h in the absence of applied stress in the temperature range from 593 to 816^{o}C. A number of discrete carbide particles $M_{23}C_6$ (rich in Cr and/or Mo) were found in intragranular region. After 8000 h aging, the distribution of grain boundary carbides was continuous with increased size. Kirchhofer et al. [14] published a paper that provided Time-Temperature-Transformation (TTT) diagram for Alloy 617. The aging temperature ranged from 500^{o}C to 1000^{o}C for times from 0.5 h to 1000 h producing a total of 70 aging conditions. Another group of materials were obtained after 10,000-30,000 h at 900^{o}C. Bruch et al. [15] examined the tensile properties of several solution-treated alloys including alloy 617 in the temperature range from 20 to 1000^{o}C. The research showed the dependence between strength parameters and strain rate at

relatively higher temperature (>700^{o}C), and related strain rates to maximum stress by Norton creep equation.

Alloy 230 is considered as a potential candidate material for the VHTR IHX. However, available data for aging effect study are limited. Kim et al. [16] studied high temperature aging effects on Alloy 617 an Alloy 230 in an impure helium atmosphere. Specimens were aged at 1000^{o}C in the impure helium containing CO, CO_2, CH_4 and H_2O for 500 h. The authors reported a steep increase in room temperature ductility and extensive carbide growth was observed below the carbide-free zone. Chatterjee et al. [17] evaluated creep behavior and microstructual details of Alloy 230. The formation of Ni_2 (Cr, W) and precipitation of Ni_3W_3C and $Cr_{23}C_6$ influences the mobility of dislocation. They also noticed that dislocation glide, subgrain formation and recrystallization made the creep deformation unstable. Gosse et al. [18] measured Chromium activity in Alloy 617, Alloy 230, and model alloys. The authors reported chromium activity in Alloy 230 was higher than in Alloy 617 and model alloys. The paper also gave new insight in the surface kinetics of both alloys though HTMS results.

Kun Mo et al. [19] in our research group led the high temperature (900^{o}C and 1000^{o}C) aging study on Alloy 617 and Alloy 230 up to 3000 h. Fine coherent $M_{23}C_6$ precipitates nucleated and coalesced on high angle grain boundaries as the aging time expending. One of the most important features of the long-termed aged alloys is the coarsening of intrinsic carbides. Further research on long-term aging (10,000 h) effects in Alloy 617 and Alloy 230 will be presented in the thesis.

Chapter 2 – Overview of Mechanical Properties and Microstructure Characters

An overview of the mechanical properties and the microstructure of Alloy 617 and Alloy 230 is presented in this chapter. The materials in this study were aged for 10,000 hours at 900^{o}C and 1000^{o}C. This divides these materials in four groups: two materials at two aging temperatures. The mechanical properties were evaluated by tensile test at 10^{-3}/s strain rate from room temperature up to 1000^{o}C. Strain-rate sensitivity analysis was conducted to properly predict the long-term flow stress. Microstructural examination covers untested and tensile tested specimens to reveal the deformation and fracture mechanisms. Scanning Electron Microscope (SEM) and Electron Backscatter Diffraction (EBSD) results were evaluated and analyzed.

2.1 Microstructure Overview

The original Alloy 617 was provided by Haynes international, Inc. in 1 inch plate, which was hot worked and solution heated at 1177^{o}C for 37 min. (Heat Number: 861758808). The original Alloy 230 used for aging was also supplied by Haynes international, Inc. in 1.5 inch plate with hot work and solution heat processing at 1191^{o}C for 3 hours (heat Number: 830587801). Then these materials were aged in VULCAN^{TM} 3-350 furnaces at 900^{o}C and 1000^{o}C for 10,000 hours, respectively. The microstructural analysis was conducted with a 7000F SEM coupled with EBSD applications and Energy Dispersive X-ray Spectroscopy (EDS). The SEM specimens were polished down to 0.05 micron with SiC abrasive paper and alumina solutions, and etched for ~3.5 min using a 10 ml HNO_3,

15ml HCl and 10 ml CH_3CO_2H mixture solution. The EBSD specimens were polished down to 0.05 micron and followed with vibratory polishing to 0.02 micron. The chemical composition of both alloys is shown in Table 2.1

Table 2.1 Chemical Composition (Weight %) [7, 9]

Elements	Alloy 617	Alloy 230
Ni	44.5 min	57.0 as balance
Cr	20.0-24.0	20.0-24.0
Co	10.0-15.0	5.0 max
Mo	8.0-10.0	1.0-3.0
Al	0.8-1.5	0.2-0.5
C	0.05-0.15	0.05-0.15
Fe	3.0 max	3.0 max
Mn	1.0 max	0.3-1.0
Si	1.0 max	0.25-0.75
S	0.015 max	0.015 max
Ti	0.6 max	0.1 max
Cu	0.5 max	0.5 max
B	0.006 max	0.015 max
P		0.03 max
La		0.05 max
W		13.0-15.0

Alloy 617 is rich in Chromium, Cobalt, and Molybdenum, and Alloy 230 is rich in Chromium, Cobalt and Tungsten. These notable elements have some notable effects in Nickel-based superalloys both in mechanical properties and microstructral features. Table 2.2 summarizes the effect of these elements.

Table 2.2 Effects of notable elements in superalloys [20]

Elements	Effects on Nickel Based Superalloys
Cr	• Improves hot corrosion and oxidation resistance • $M_{23}C_6$ and M_7C_3 carbide precipitation • Moderate solid-solution hardening • Moderate increase in γ' volume fraction • Promotes tcp phases
Mo	• High solid-solution hardening • Moderate increase in γ' volume fraction • M6C and MC carbide formation • Promote tcp phases (σ, μ)
W	• High solid-solution hardening • Moderate increase in γ' volume fraction • M_6C carbide formation • Promote tcp phases (σ, μ)
Co	• Raises γ solidus temperature • Moderate increase in γ' volume fraction (some alloys) • Raises γ' solves temperature

Alloy 617 and Alloy 230 are polycrystalline, as shown in the figures below, grains and intrinsic particles were observed clearly. The major intrinsic particles in Alloy 617 are Cr rich $M_{23}C_6$, Mo rich M_6C, and Ti(C, N), and those in Alloy 230 are Cr rich $M_{23}C_6$ and W rich M_6C carbides. [21] Fig 2.1 and Fig 2.2 show the microstructures of Alloy 617 and Alloy 230 at different aging temperatures. Inclusion particles in Alloy 617 are not evenly distributed compared to Alloy 230, and they agglomerate and form "clouds." Smaller grains are located in the inclusion rich area, and larger grains are found in inclusion free area. This duplex grain size distribution is due to Zener pinning. Zener pinning denotes

the effects of fine particles on grain boundary movement. These particles exert pinning pressure counteracting the driving force for boundary movement, which is very important on grain growth.

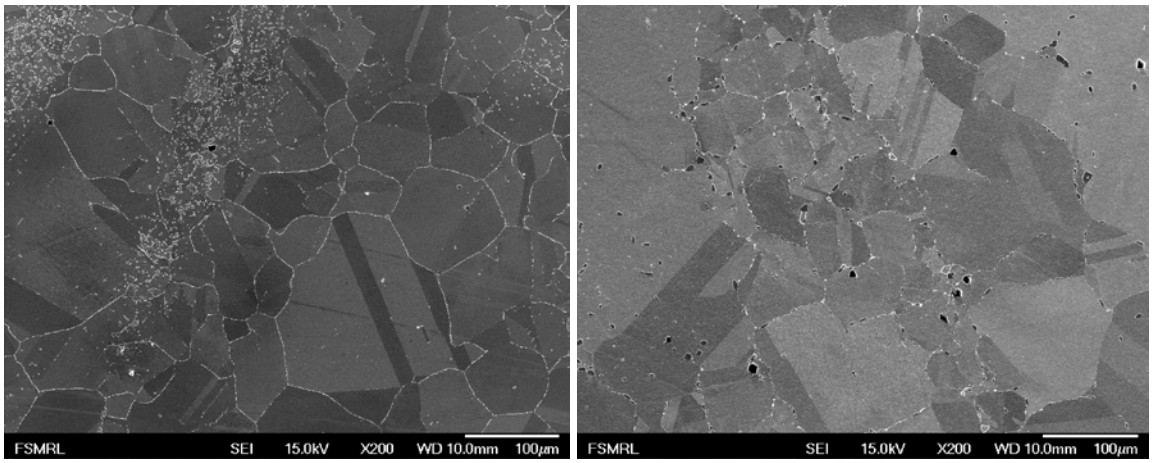

(a) (b)

Fig 2.1 Microstructure overviews of long-term aged Alloy 617: (a) 10,000 h aged Alloy 617 at 900^{o}C (b) 10,000 h aged Alloy 617 at 1000^{o}C

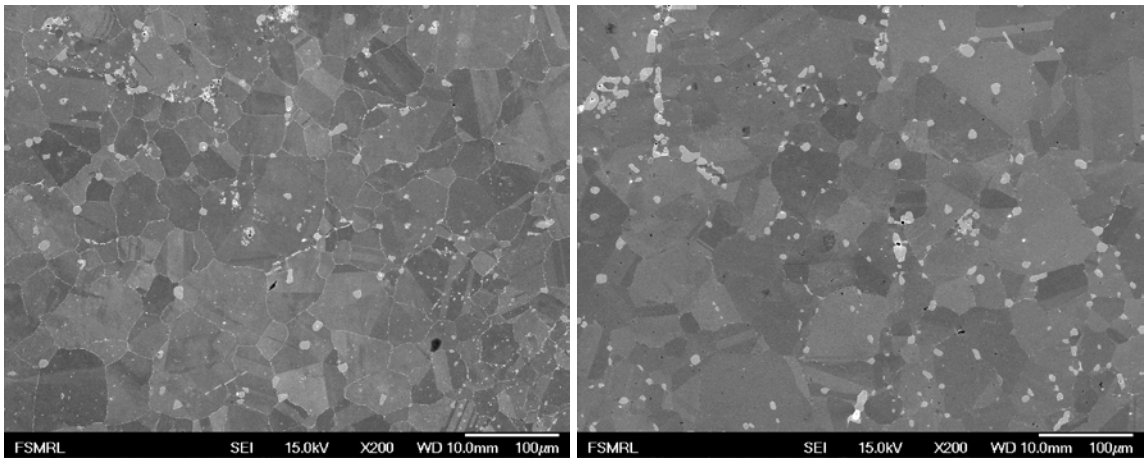

(b) (d)

Fig 2.2 Microstructure overviews of long-term aged Alloy 230: (a) 10,000 h aged Alloy 230 at 900^{o}C (b) 10,000 h aged Alloy 230 at 1000^{o}C

Distributions and geometry of intrinsic particles that are formed at the grain boundaries vary with different aging temperature. Fig 2.3 and Fig 2.4 show grain particles along the grain boundaries.

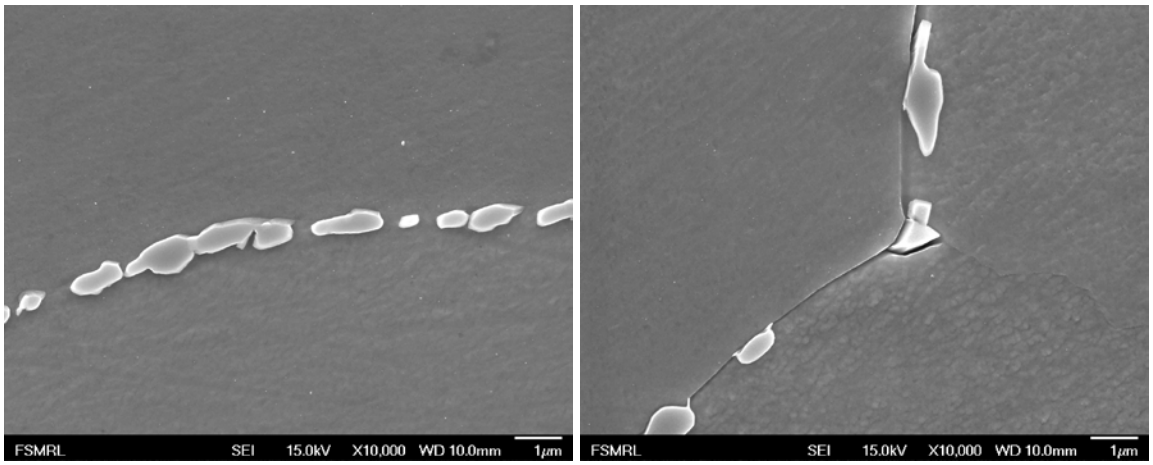

(a) (b)

Fig 2.3 Intergranular particles in Alloy 617: (a) 10,000 h aged Alloy 617 at 900^{o}C (b) 10,000 h aged Alloy 617 at 900^{o}C

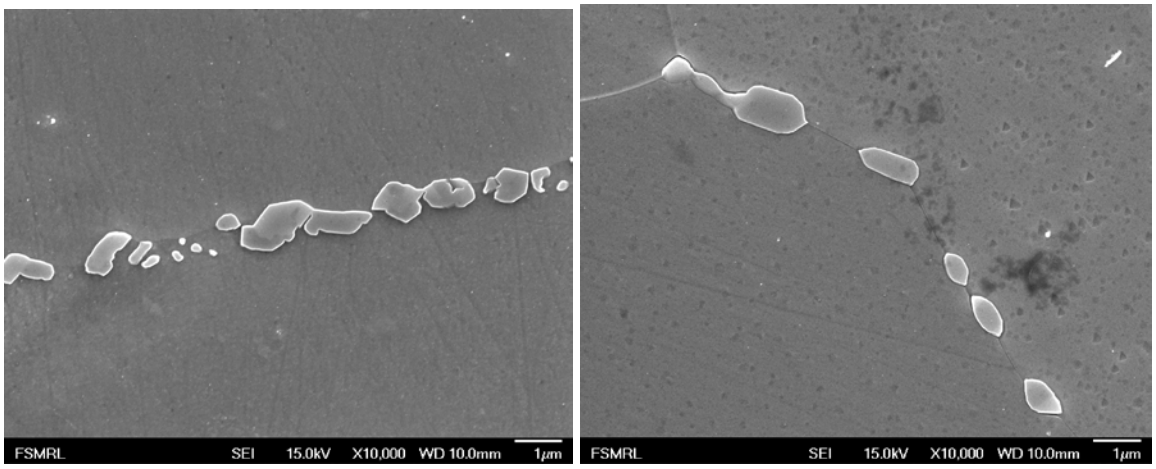

(a) (b)

Fig 2.4 Intergranular particles in Alloy 230: (a) 10,000 h aged Alloy 617 at 900^{o}C (b) 10,000 h aged Alloy 617 at 900^{o}C

Intergranular particles in the as-received alloys are thin film precipitates. In contrast, the distributions of intergranular particles for long-term aged alloys are different: at lower aging temperature (900^{o}C), most of the particles are connected and form band-like clusters; when the aging temperature is higher (1000^{o}C), the coarsening of intergranular particles is obvious and spacing is larger. Particles coarsening during the aging periods will be evaluated and discussed in next chapter.

An overview EBSD analysis is presented in the Fig 2.5 and Fig 2.6. ~58% and ~60% of the grain boundaries are twin boundaries (Coincidence Site Lattice (CSL) Σ3 grain boundaries) for 900^{o}C and 1000^{o}C long-term aged Alloy 617, and 54% and 57% of the grain boundaries are twin boundaries for 900^{o}C and 1000^{o}C long-term aged Alloy 230. The twin boundary fractions are slightly higher than as-received alloys.

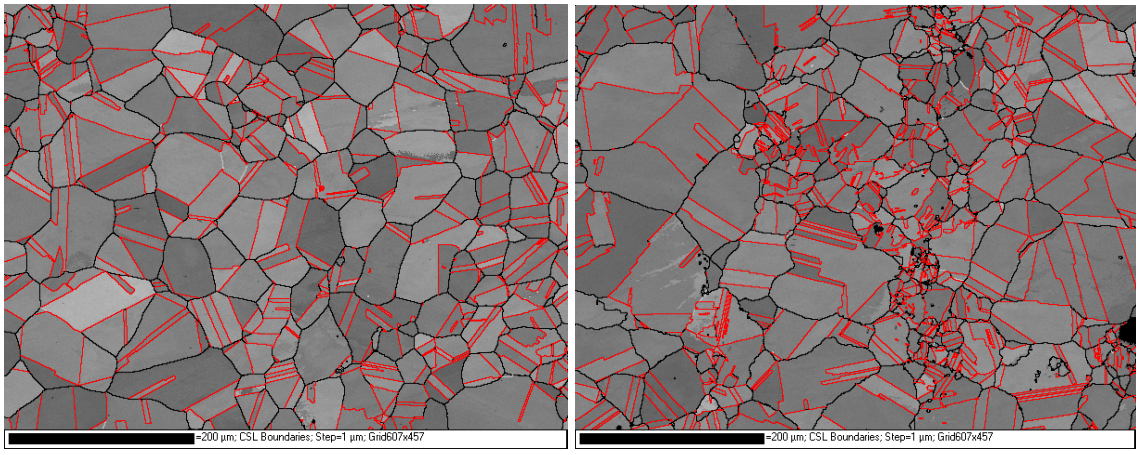

(a) (b)

Fig 2.5 CSL boundary analysis of Alloy 617: (a) 10,000 h aged Alloy 617 at 900^{o}C (b) 10,000 h aged Alloy 617 at 1000^{o}C

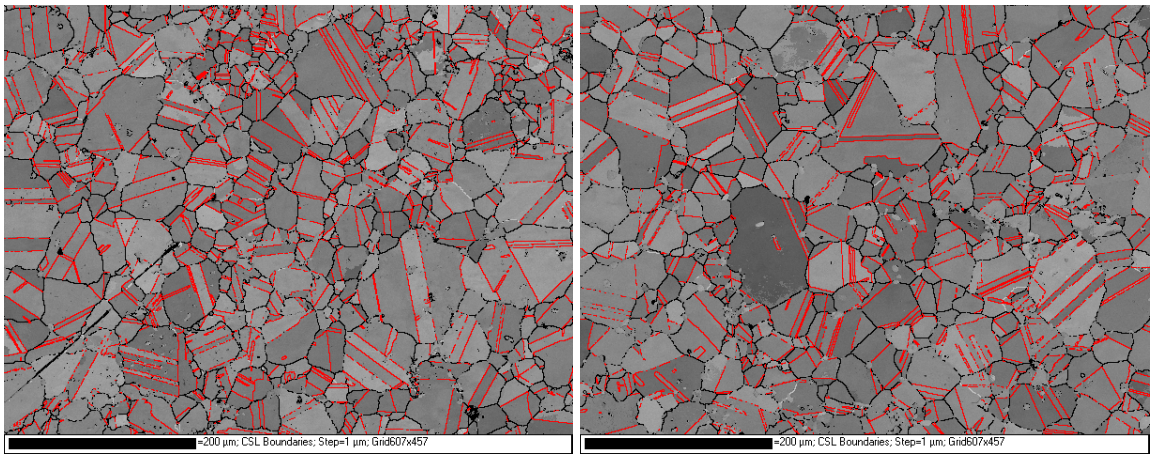

(a) (b)

Fig 2.6 CSL boundary analysis of Alloy 230: (a) 10,000 h aged Alloy 230 at 900^{o}C (b) 10,000 h aged Alloy 230 at 1000^{o}C

2.2 Mechanical Tests

The tensile test specimen configurations and test results are presented in this section. These tensile tests were conducted at strain rate ~10^{-3}/s using an INSTRON 131servo-hydraulic test system equipped with a high temperature furnace at Advanced Materials Testing and Evaluating Laboratory (AMTEL). The temperature ranges form room temperature (RT) to 1000^{o}C and was maintained for ~40 min to gain relatively smoothly distributed temperature zone in the furnace. The maximum overshoot of temperature was 10^{o}C and the variation around temperature set point was less than 2^{o}C.

In order to mimic the real working conditions of these structural materials in an IHX (requires the thickness of tested materials to be in the range from 0.2 to 2mm) [22], the size and geometry are chosen with comparable dimensions. Tensile tests of these alloys using specimens with the same dimensions have been used in previous research [19].

This specimen design is also convenient for conducting sufficient tests with limited amounts of material. These tensile specimens were cut in long-transverse direction in the rolling plane. (Fig 2.7)

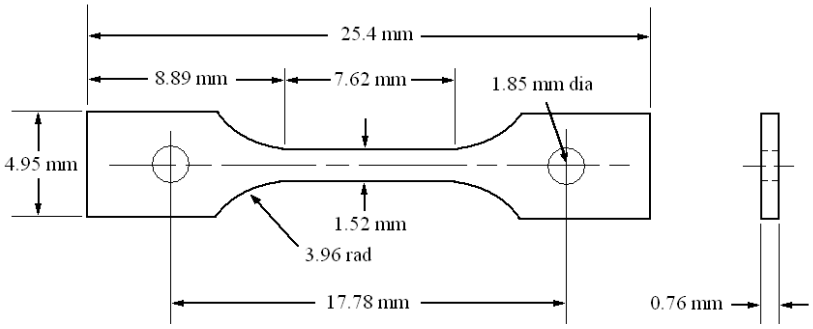

(a)

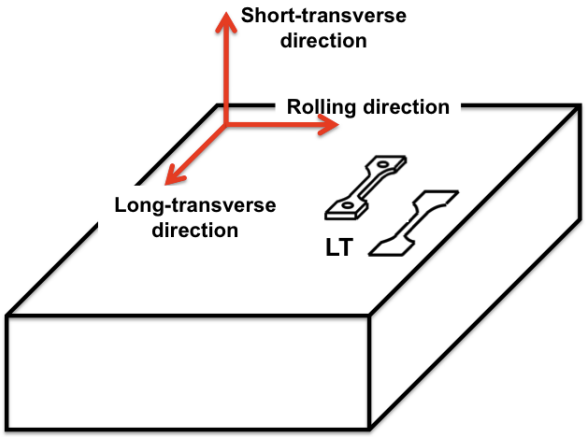

(b)

Fig 2.7 Tensile specimens: (a) Geometry and dimension (b) Sampling direction

The results of tensile tests are summarized and labeled in Fig 2.8 and Fig 2.9. Both long-term aged Alloy 617 and Alloy 230 show similar mechanical properties feature changes at elevated temperature. At room temperature, both alloys have high strength that can withstand high stresses during tensile loading. The stresses experience a moderate decrease when the temperature reaches 200^{o}C. A slight change in tensile strength is found

in the temperature range of 200°C to 700°C. When temperature is increased up to 800°C, a significant weakening of strain hardening can be seen, and little if any strain hardening phenomena are observed from the strain-stress curve at 900°C and 1000°C.

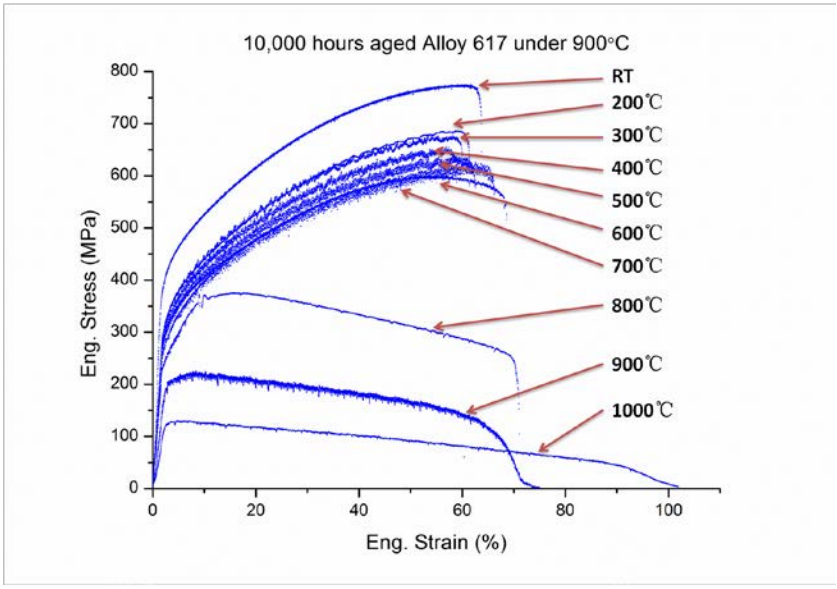

(a)

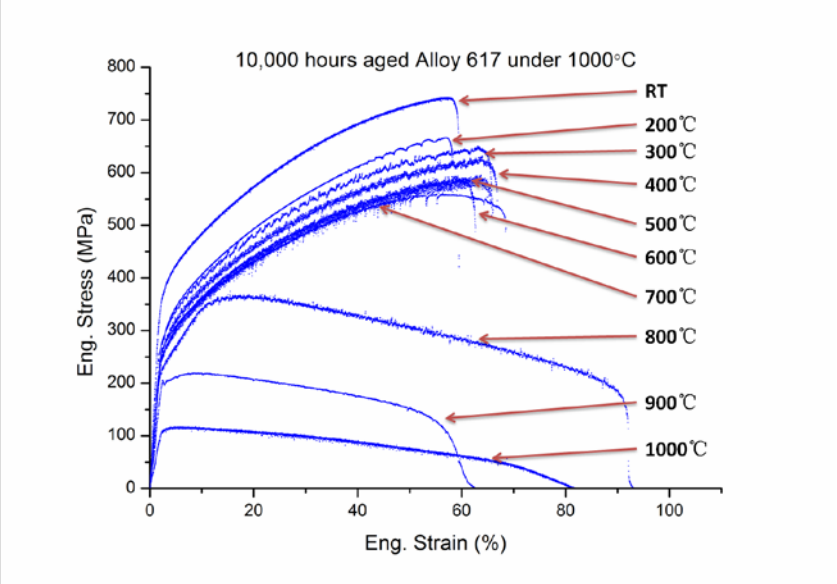

(b)

Fig 2.8 Strain-stress curves for Alloy 617: (a) 10,000 h aged Alloy 617 at 900°C (b) 10,000 h aged Alloy 617 at 1000°C

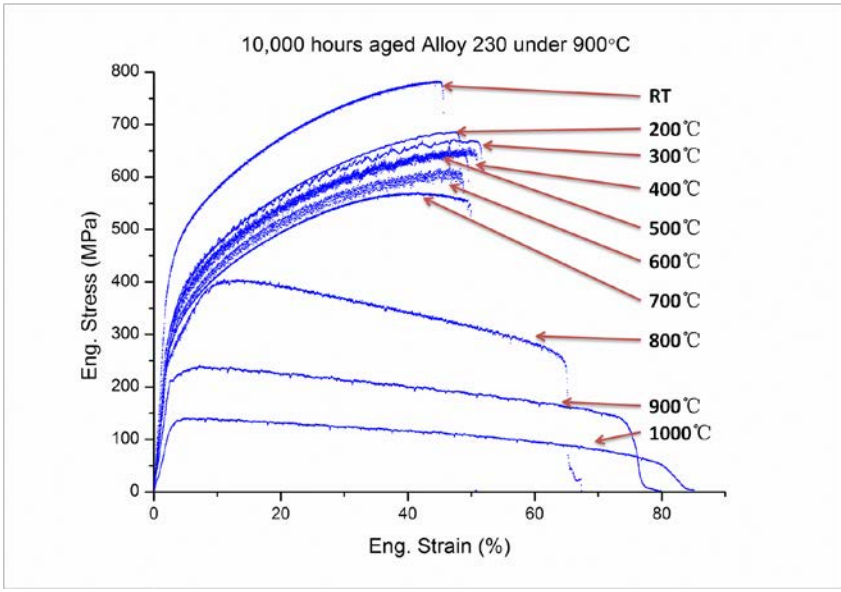

(a)

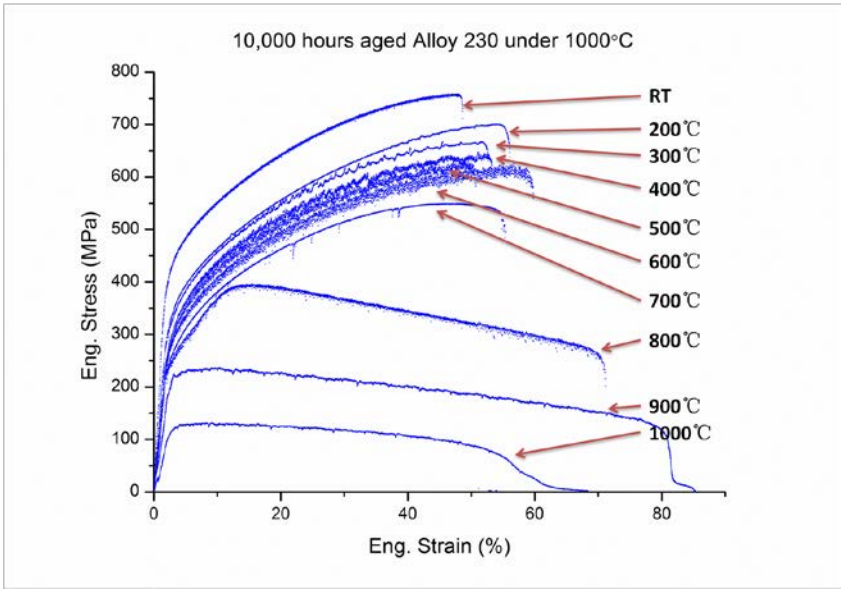

(b)

Fig 2.9 Strain-stress curves for Alloy 230: (a) 10,000 h aged Alloy 230 at 900^{o}C (b) 10,000 h aged Alloy 230 at 1000^{o}C

Since there are significant differences between the lower temperature region (< 800^{o}C) and the higher temperature region (>800^{o}C), the fracture and deformation mechanisms

should be evaluate separately. Fig 2.10 presents the yield stress (Y.S.) and ultimate tensile stress (U.T.S.) at different temperatures for long term-aged Alloy 617 and Alloy 230. A steep decrease of U.T.S. was observed at temperatures greater than 700°C.

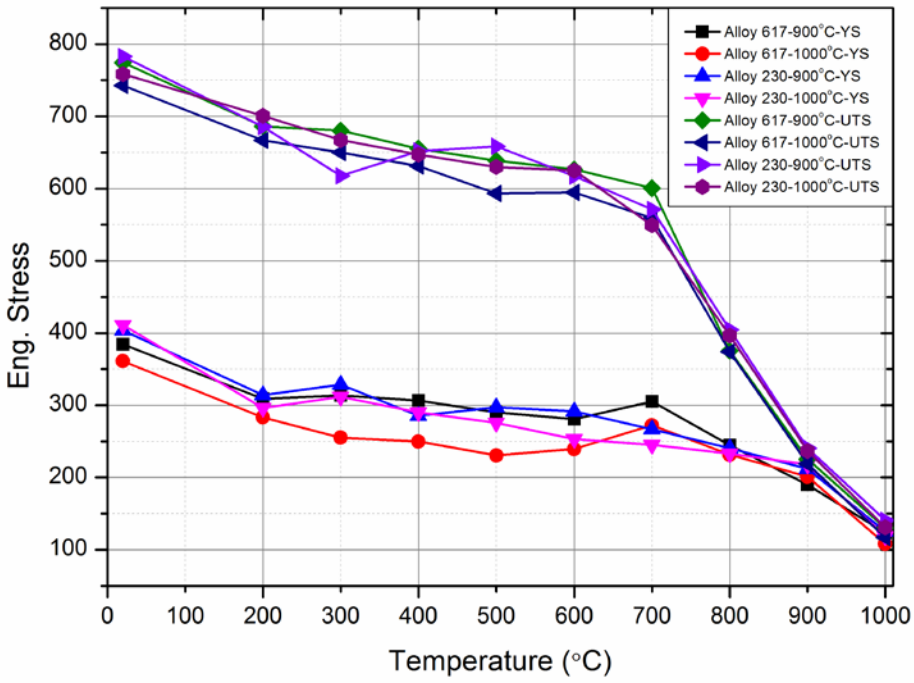

Fig 2.10 Yield Stress (Y.S.) and Ultimate Tensile Stress (U.T.S.) of Long-term aged Alloy 617 and Alloy 230

2.2.1 Tensile response in the lower temperature region (Room temperature to 700°C)

The fracture mechanisms for tensile tests conducted at temperatures below 800°C were carefully investigated. Cavities initiate because particles do not deform, and therefore force the matrix around the particles to deform more than average. This, in turn produces a higher stress near the particles. When the stress is large enough, the matrix-particle

interface may separate or particle itself may crack [23]. Fig 2.11 shows intrinsic particle cracks for room temperature tensile test specimens. The coalescence of voids finally results in premature failure and only a small amount of elongation beyond necking point.

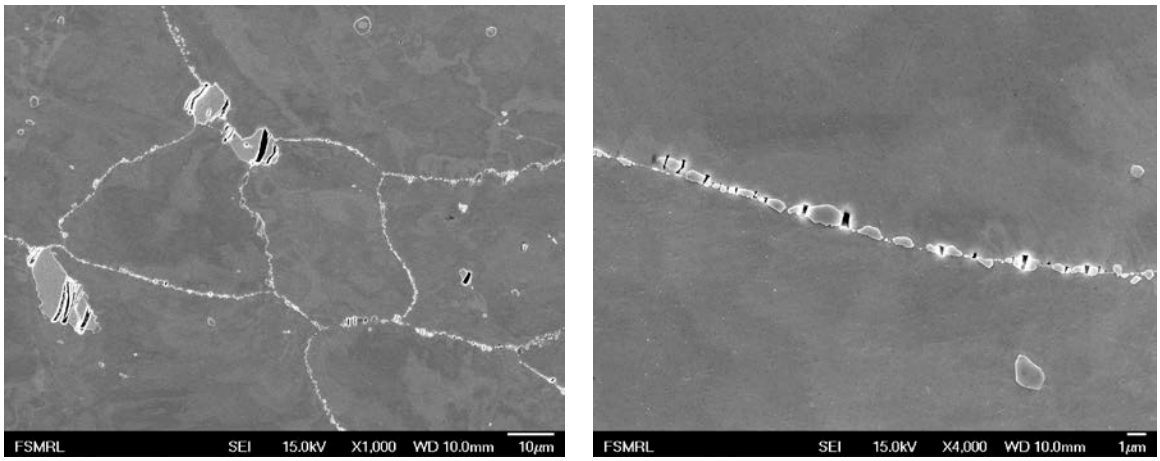

(a) (b)

Fig 2.11 Intrinsic particles crack after room temperature tensile test: (a) Inclusion (b) Intergranular particles

Fractography also reveals that the particle fracture induces transgranualar fracture in both alloys. Fig 2.12 shows the fractography for aged Alloy230 aged after a room temperature tensile test. The individual grains can be identified and dimples with equiaxed microvoids can be found in the image. A closer view of carbides is presented in Fig 2.13. Intrinsic carbide fracture can be seen for both alloys in the picture (Fig 2.16). The phenomenon is very important in interpreting further mechanical properties change during the aging process. These carbides are identified by EDS, and detailed information will be discussed in the next section.

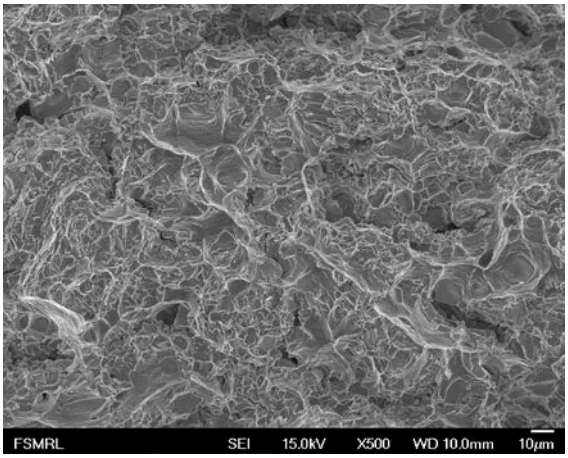

Fig 2.12 Fractography for Alloy 230

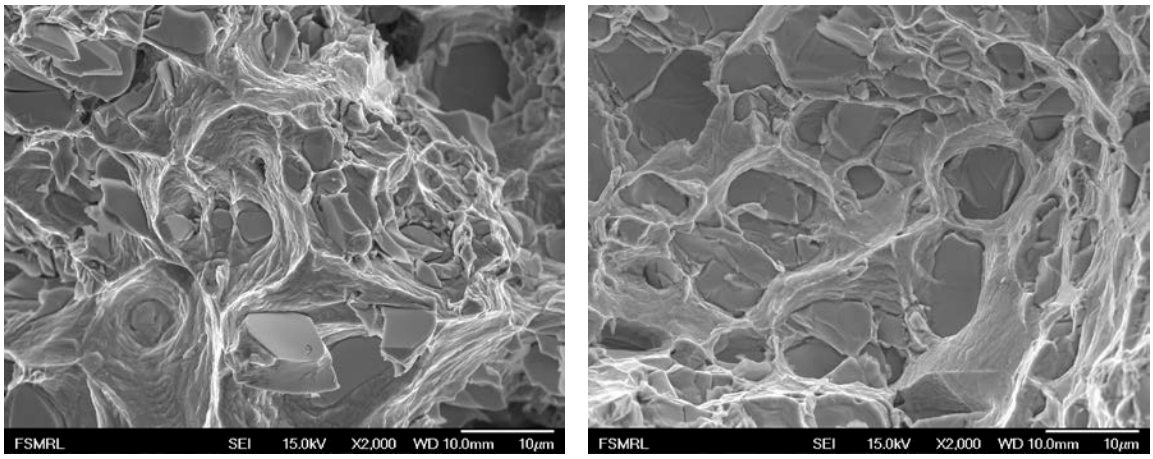

(a) (b)

Fig 2.13 Carbides fracture: (a) Alloy 230 (b) Alloy 617

Another main feature of tensile response in the lower temperature region is the Portevin-LeChatelier effect. At room temperature, the stress-strain curve is smooth and stable. As the test temperature increases, the stress-strain curves lose stability and become serrated. Solute atoms that have high mobility (e.g. carbon atoms) block the dislocation movement of dislocations during plastic deformation, and are released when higher external stress is

applied. The “impede and release” process repeats and shows up as the serrated behavior in the strain-stress curves. Since the process occurs as a function of temperature and strain rate during external loading, this phenomenon is called dynamic strain aging.

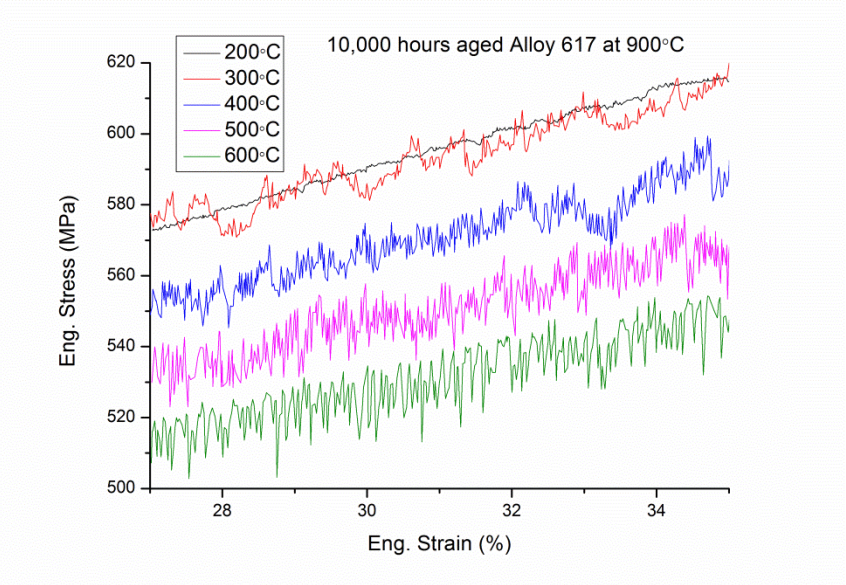

(a)

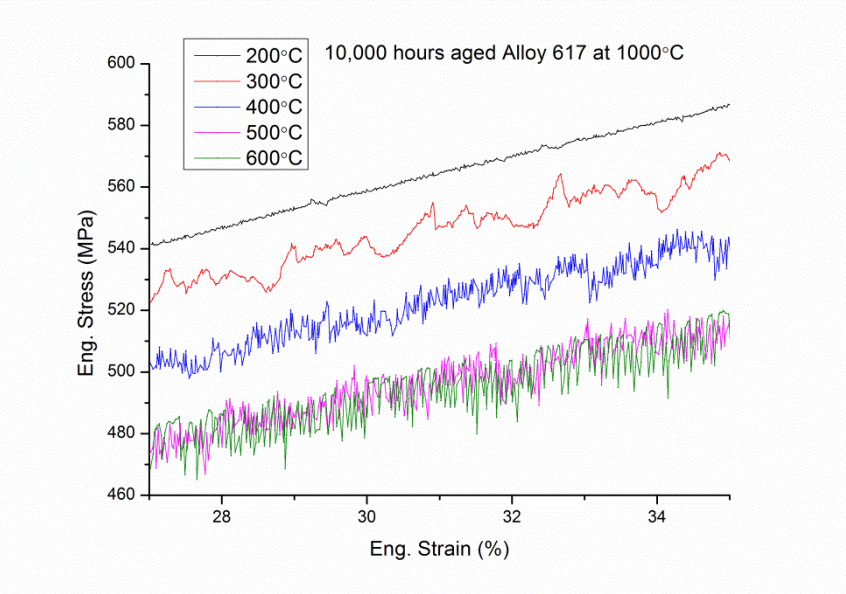

(b)

Fig 2.14 Portevin-LeChatelier effect: (a) 10,000 h aged Alloy 617 at 900^{o}C (b) 10,000 h aged Alloy 617 at 1000^{o}C

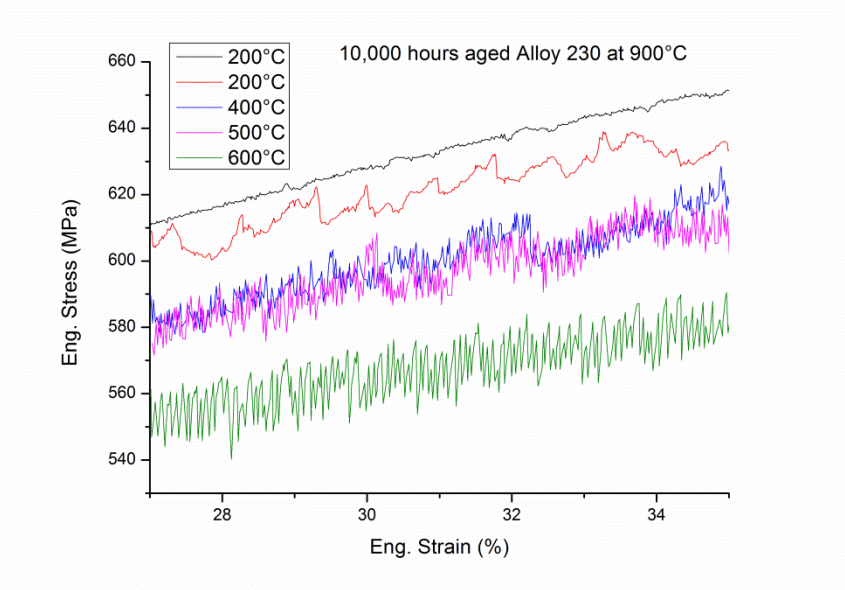

(a)

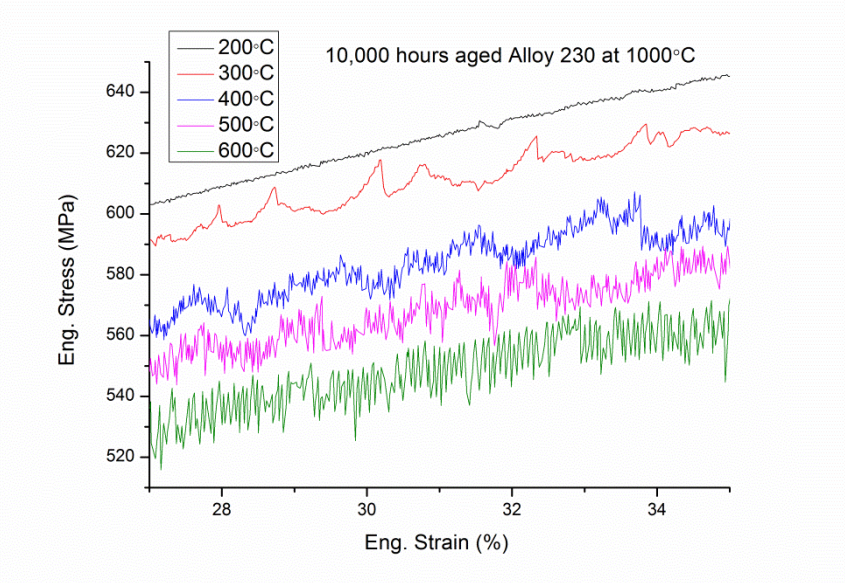

(b)

Fig 2.15 Portevin-LeChatelier effect: (a) 10,000 h aged Alloy 230 at 900^{o}C (b) 10,000 h aged Alloy 230 at 1000^{o}C

Fig. 2.14 and Fig. 2.15 show the Portevin-LeChatelier effect on both alloys. The amplitude of serration is increasing due to the higher atom diffusible ability at elevating temperature. Table 2.3 shows the amplitude of serration in these curves.

Table 2.3 Amplitude of stress oscillations (MPa)

Temperature (^{o}C)	300	400	500	600
Alloy 617 (900^{o}C aged)	14	15	16	18
Alloy 617 (1000^{o}C aged)	11	13	15	16
Alloy 230 (900^{o}C aged)	11	13	16	19
Alloy 230 (1000^{o}C aged)	12	16	17	20

2.2.2 Tensile response in the higher temperature region (800^{o}C to 1000^{o}C)

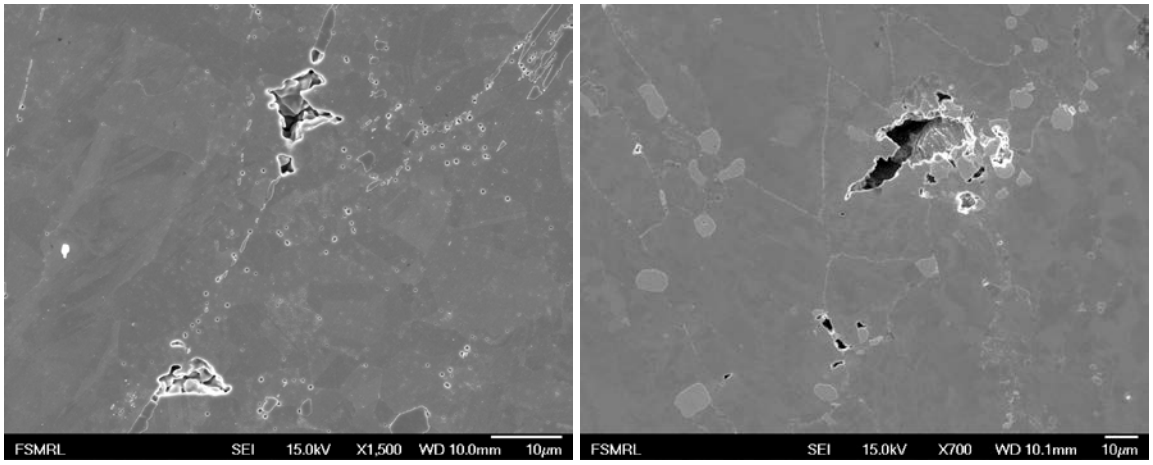

(a) (b)

Fig 2.16 Fracture Mechanisms at 900^{o}C: (a) Round cavities in grains and cracks at grain boundaries (b) Cracks at inclusion particles

The analysis in higher temperature region is more complex than the lower temperature region since additional fracture mechanisms and loss of strain hardening are involved. For both long-term aged Alloy 617 and Alloy 230, 800^{o}C could be considered as "equicohesive temperature", above which dislocation movement will not be impeded by grain boundaries. [24] At temperature higher or equal to 800^{o}C, the particle pinning

mechanism is not efficient in since most of the dislocations with enhanced mobility are able to bypass the particles by dislocation creep. [25] In addition, the process of dynamic recrystallization releases stress at intrinsic particles. Fig 2.16 shows cavities in long-term aged specimens: round cavities are observed in grains and at intergranular particles in Alloy 617, and cavities concentrated at inclusion particles in Alloy 230.

Dynamic recrystallization (DRX) is another mechanism observed during high temperature plastic deformation. EBSD analysis was applied to differentiate recrystallized grains and original grains. DRX is defined as the recrystallizaion that take place during high-temperature deformation. Two board classes of DRX can be classified based on whether the process involves nucleation or not. The first one is discontinuous dynamic recrystallization (DDRX), or simply referred to as "dynamic recrystallization." This process involves nucleation and growth of new grains. The second one is the continuous recreystallizaion (CDRX), which does not involve nucleation and results from migration of grain boundaries [26]. It is well known that DDRX always happens in low to medium stacking fault energy materials (e.g. nickel based alloys). In this case, dynamic recovery is not efficient in recovering local stress concentrations so that high local gradients of dislocation density drive large grain boundary immigration. In contrast to DDRX, high stacking fault energy materials always undergoes the CDRX process. Since the dynamic recovery is efficient, the driving force to produce large dislocation density gradients is weak. In this case, then the dislocations tend to form subgrain boundaries (misorientation angle $<15^{o}$), and some of the dislocation wall continuously

transformed to high angle boundaries (misorientation angle >15^{o}) [27]. The main features of CDRX and DDRX are summarized in Table 2.4

Table 2.4 Main Features of CDRX and DDRX [28]

	CDRX	**DDRX**
Generation	Occurs by transformation of sub grain or low-angle boundaries into grain or high-angle boundaries	Occurs by local cycles involving strain hardening, then nucleate and form new grains
Dynamic recovery	Strong (dislocation rearrangement or annihilation)	Weak
Dislocation	Homogeneous	Inhomogeneous
Grain boundary	Rate of migration is low	Rate of migration is high

Temperature dramatically influences the activation of DRX and subsequent grain growth. Higher temperatures will enhance thermal fluctuation that results in a higher probability of successful activation. Grain growth occurs by migration of grain boundaries, and the diffusion rate is enhanced with elevated temperature. Fig 2.17 and Fig 2.18 show representative the EBSD images at different temperatures and DRX grain area fractions over a scanned area for 1000^{o}C long term aged Alloy 617 (near fracture surface), respectively.

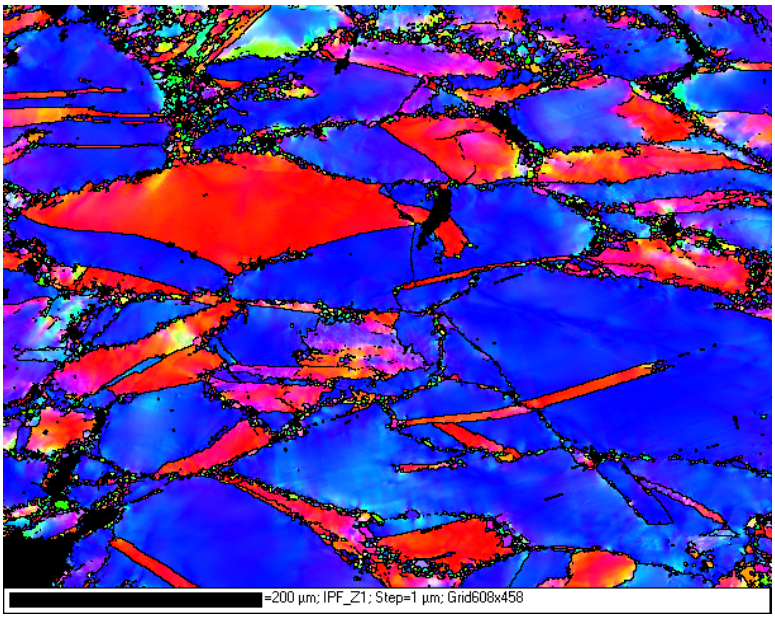

(a)

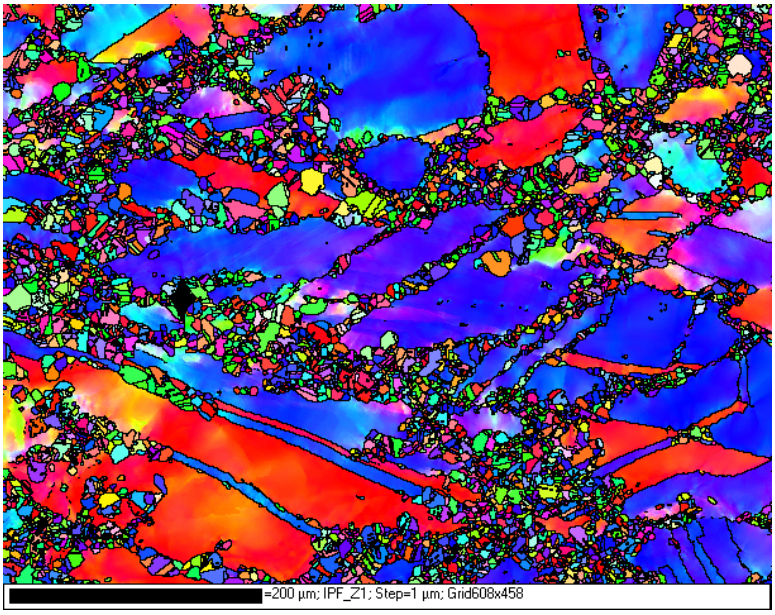

(b)

Fig 2.17 EBSD image of 1000^{o}C long term aged Alloy 617 at different study temperatures: (a) 800^{o}C (b) 900^{o}C (c) 1000^{o}C

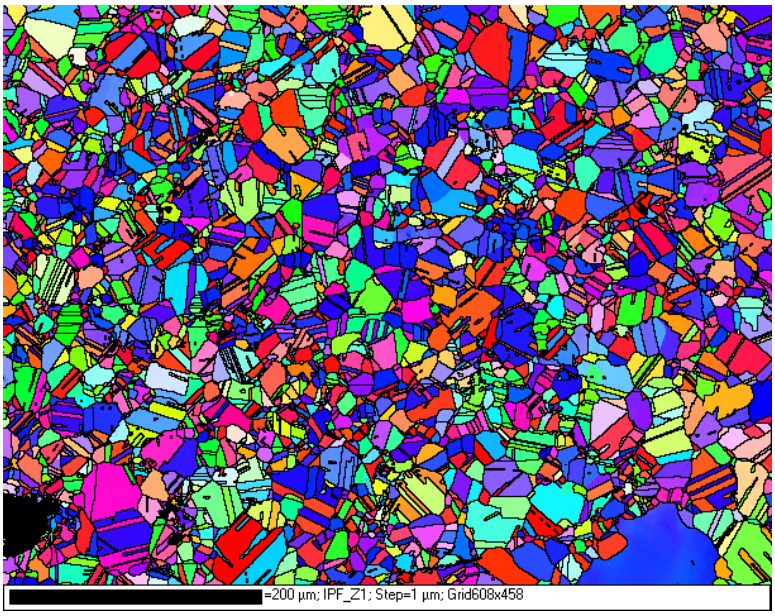

(c)

Fig 2.17 (cont.)

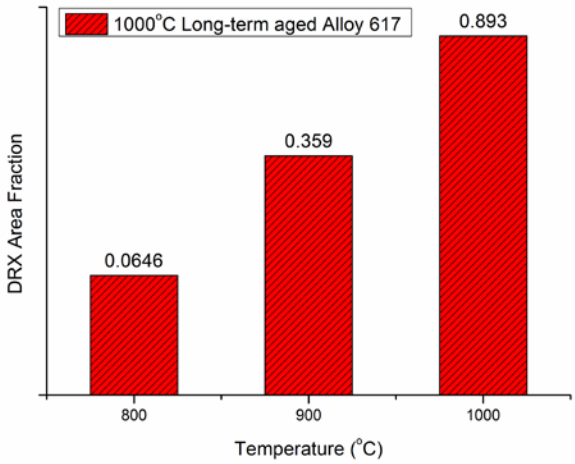

Fig 2.18 DRX area fraction of 1000°C long term aged Alloy 617 at different study temperatures

DRX initiates at grain boundaries where high densities of dislocations are available. The deformed or original grains are decorated with small recrystallized grains in a necklace-

like distribution at 800^{o}C. As the hold time or temperature increases, the small recrystallized grains grow and consume the original large grains through a process of grain boundary migration. Since the newly generated recrystallized grains are randomly oriented, the texture of deformed specimens will change. The texture analysis was performed using EBSD techniques. Fig 2.19 shows the chamber configuration. It should be noted that the direction marked “RD” should be transverse direction since the tensile axis is parallel to the “rolling direction” marked in the holder.

Pole figures show a statistic summary of the grain orientation in a specific area, and it reflects the texture change due to the DRX. Fig 2.20 shows the pole figures of the 1000^{o}C long-term aged Alloy 617 after corresponding tensile loading. For the 800^{o}C tensile test, the recrystallized area is limited to regions along the grain boundaries which only contribute about ~6.5% area fraction. The duplex texture of the tested specimen is <111>+<001>. When the temperature is higher, the material will lose the as-rolled texture and exhibit a more homogeneous orientation distribution. Similar phenomena are also found in Alloy 230.

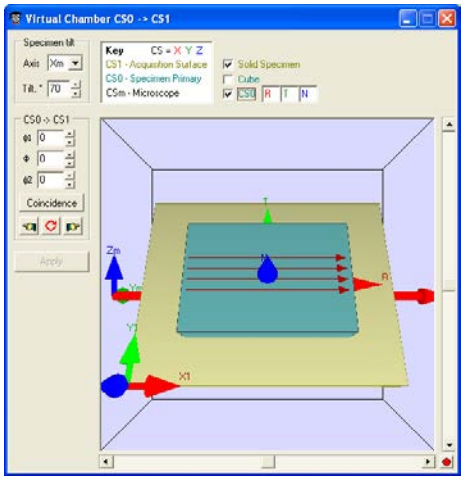

Fig 2.19 Chamber configuration

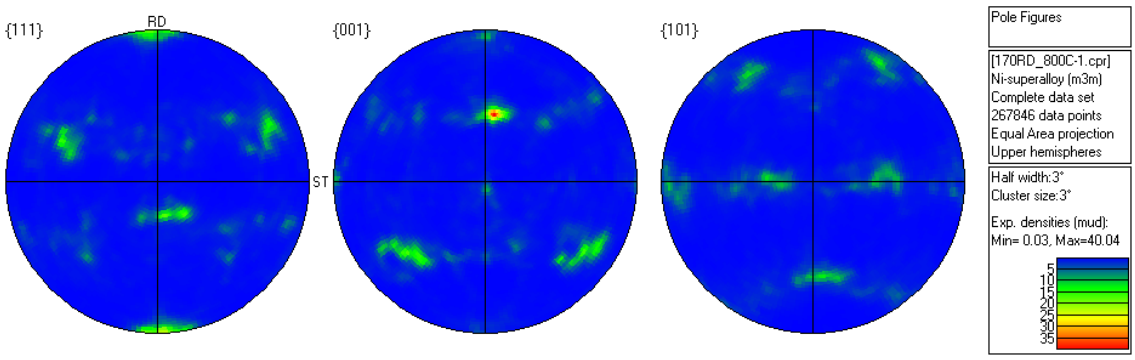

(a)

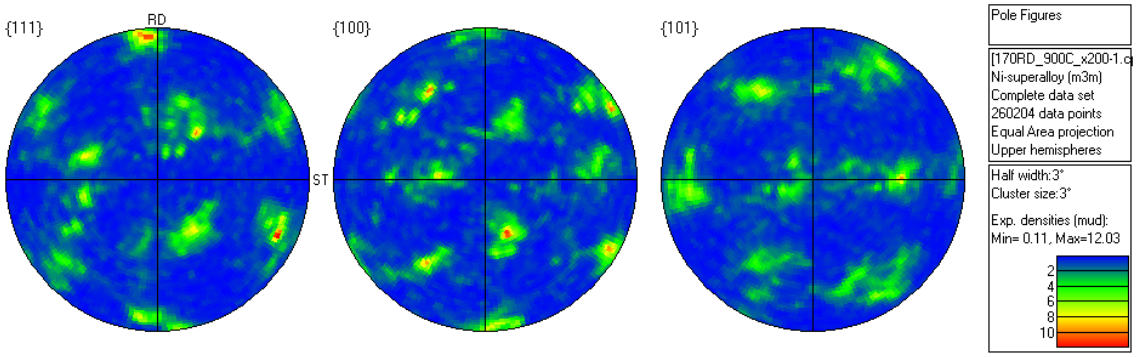

(b)

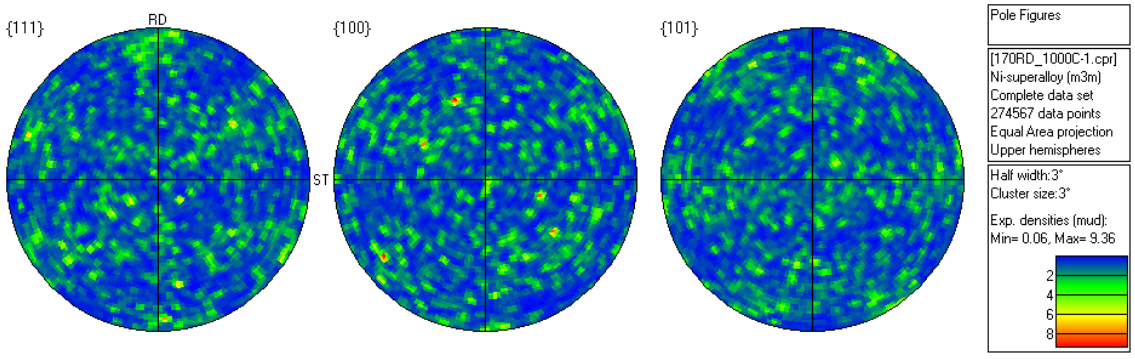

(c)

Fig 2.20 Pole figures for 1000^{o}C long term aged alloy 617 after tensile tests at (a) 800^{o}C (b) 900^{o}C (c) 1000^{o}C

2.2.3 Strain rate sensitivity analysis

Strain rate has a significant influence on the value of the flow stress measured in tensile tests. For most metallic materials, the magnitude of flow stress is proportional to the strain rate. The strain rate dependent flow stress phenomenon is also affected by temperature. In other words, flow stress is more sensitive to strain rate at higher temperature in most cases. A parameter that describes and evaluates the strain rate effects is the strain rate sensitivity. Alloys 617 and 230 are proposed for use as structural materials that work at high temperature, so knowledge of the strain rate sensitivity is essential.

The strain rate sensitivity is evaluated by the parameter m, which is related to strain rate, $\dot{\varepsilon}$, in the following way.

$$\sigma_t = C(\dot{\varepsilon})^m \tag{3-1}$$

The strain rate is defined as $\dot{\varepsilon} = d\varepsilon_t / dt$ in the unit of s^{-1}, where ε_t is true strain. The engineering strain-engineering stress curve if found directly from the tensile test results, the relationship between true strain (ε_t)-true stress (σ_t) and engineering strain (ε_e)-engineering stress (σ_e) and be described as:

$$\sigma_t = \sigma_e(1+\varepsilon_e) \tag{3-2}$$

$$\varepsilon_t = \ln(1+\varepsilon_e) \tag{3-3}$$

$$\dot{\varepsilon}_t = \frac{d\varepsilon_e / dt}{(1+\varepsilon_e)} = \frac{\dot{\varepsilon}_e}{1+\varepsilon_e} \tag{3-4}$$

Based on Eq. (3-1), the strain rate sensitivity, m, can be determined by:

$$\frac{\sigma_a}{\sigma_b} = \left(\frac{\dot{\varepsilon}_a}{\dot{\varepsilon}_b} \right)^m \tag{3-5}$$

Where σ_a and σ_b are the measured flow stresses during tensile testing at true strain rate $\dot{\varepsilon}_a$ and $\dot{\varepsilon}_b$, respectively. Then m can be obtained by:

$$m = \frac{\log\left(\frac{\sigma_a}{\sigma_b} \right)}{\log\left(\frac{\dot{\varepsilon}_a}{\dot{\varepsilon}_b} \right)} \tag{3-6}$$

In the previous study conducted by Kun Mo [25], the strain rate sensitivity was obtained from a single strain rate tensile test with different strain rate. The true strain rate is approximated by:

$$\dot{\varepsilon}_t = \frac{d\varepsilon_e / dt}{1+\varepsilon_e} = \frac{\dot{\varepsilon}_e}{1+\varepsilon_e} \approx \dot{\varepsilon}_e \tag{3-7}$$

The relationship is valid when the corresponding engineering strain is small. Then $\dot{\varepsilon}_t$ can be replaced by $\dot{\varepsilon}_e$ when the value is taken from the value of the stress at 0.2% yield point ($\varepsilon_e = 0.002$), as was done in that study. A better method to get the value of m is developed in this study. It is based on a triple strain rate tensile test technique. During the test, the strain rate jump is completed in a very short time so that at the jump point, the local strain is taken as constant. Then we can replace the true strain rates in Eq. (3-6) by engineering strain rate, which is very convenient to setup and measure in the tensile test system.

Sufficient data were obtained to get strain rate sensitivity by conducting triple strain rates tensile tests at $0.001s^{-1}$, $0.005s^{-1}$ and $0.01s^{-1}$. Fig 2.21 shows the stress-strain diagrams for

long-term aged Alloy 617 and Alloy 230 at 900°C and 1000°C. Three "steps" were observed in the diagram due to the sudden strain rate jump at a specific point. The value of *m* is determined by measuring the slope of $\log(\dot{\varepsilon})$ - $\log(\sigma)$ curves. Fig 2.21 shows that plastic flow reaches steady state at a constant flow stress in each strain rate region.

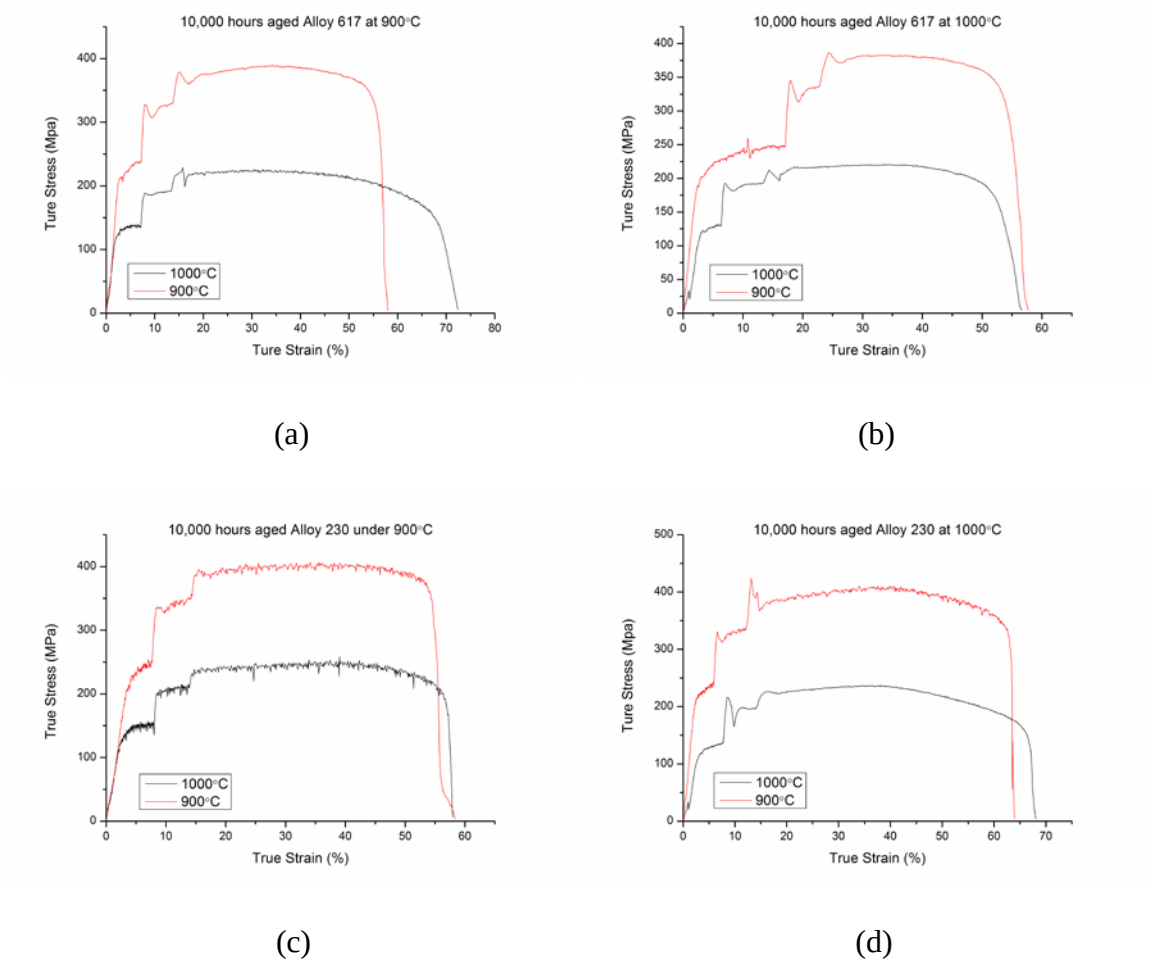

Fig 2.21 Triple strain rate tensile test results: (a) 10,000 h aged Alloy 617 at 900°C (b) 10,000 h aged Alloy 617 at 1000°C (c) 10,000 h aged Alloy 230 at 900°C (d) 10,000 h aged Alloy 230 at 1000°C

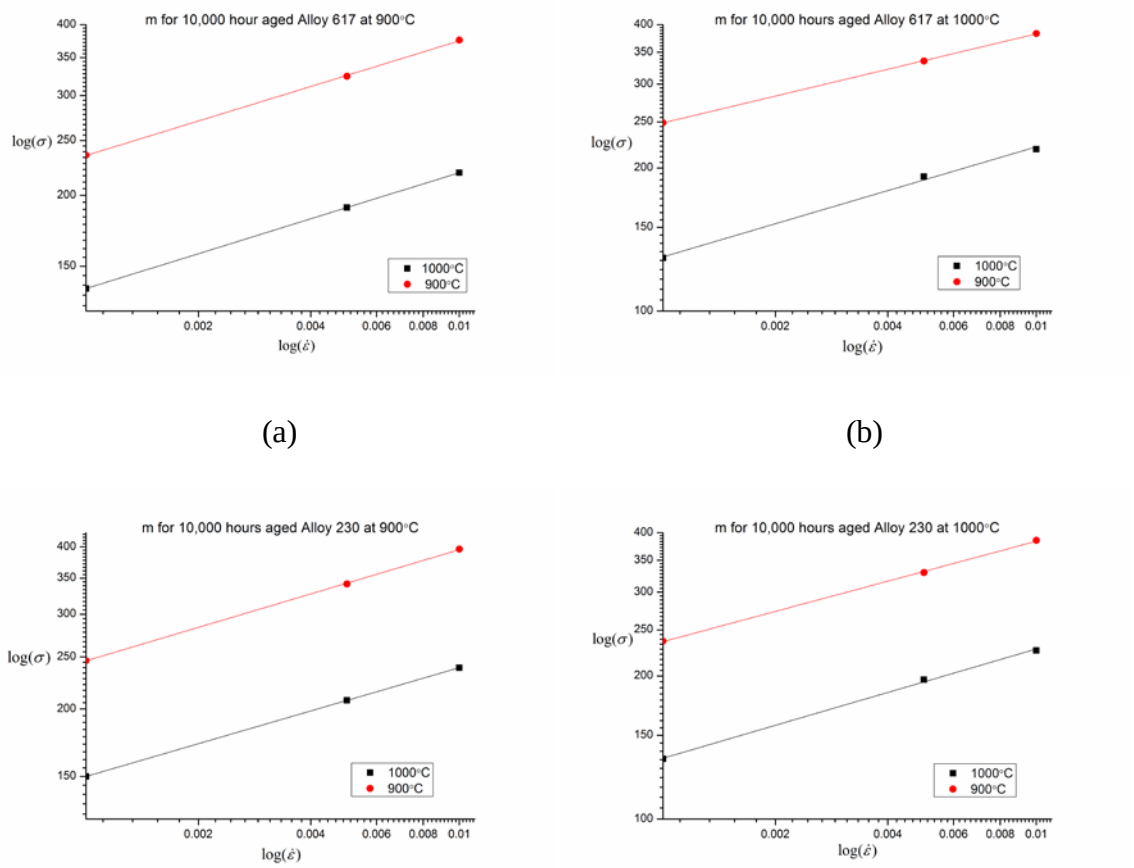

(a) (b)

(c) (d)

Fig 2.22 Linear fits of the triple strain rate tensile test results: (a) 10,000 h aged Alloy 617 at 900°C (b) 10,000 h aged Alloy 617 at 1000°C (c) 10,000 h aged Alloy 230 at 900°C (d) 10,000 h aged Alloy 230 at 1000°C

At high temperature, dislocations mobility is typically high so that they are able to climb over particles at sufficiently large applied stresses. This can result in a stable plastic flow stress. Fig 2.22 presents the linear fit results of slope and the strain rate sensitivities which are also summarized in Table 2.5. The values of the strain rate sensitivity of long-term aged Alloy 617 are closed to those of long-term aged Alloy 230. A high strain rate

sensitivity value means that a small decrease in the strain rate will lead to a large reduction in strength which is the case for both alloys.

Table 2.5 Summary of strain rate sensitivity analysis

Material	900°C	1000°C
10,000 h aged Alloy 617 at 900°C	0.20	0.20
10,000 h aged Alloy 617 at 1000°C	0.19	0.23
10,000 h aged Alloy 230 at 900°C	0.21	0.20
10,000 h aged Alloy 230 at 1000°C	0.21	0.23

The strain rate sensitivity was found to be approximately constant value for wide range of strain rates. Therefore it is possible to predict the long-term loading response from short-term material properties based on strain-rate sensitivity. The strain rate for one year operation of VHTR is $\sim 3\times10^{-10}\,s^{-1}$, and decreases to $\sim 3\times10^{-11}\,s^{-1}$, and $\sim 5\times10^{-12}\,s^{-1}$ for 60 years operation [25]. The estimated constant flow stress and ASME allowable stress for Alloy 617 is summarized in Table 2.6. The strain rate sensitivity data is retrieved from Idaho National Laboratory report [6]. It shows that at the 900°C operating temperature, the strength for Alloy 617 for a one year operation period Alloy 617 is still within the ASME allowable stresses. However, after a longer operation period, the alloy is not able to withstand the allowable stress that it will rupture within the service life. The flow stress for 1000°C operation for Alloy 617 is still within the allowable stress region.

Table 2.6 Estimated flow stress and ASME allowable stress for as-received Alloy 617

Temperature (°C)	1 Year (MPa)	10 Years (MPa)	60 Years (MPa)	ASME allowable stress (MPa) [25]
900 (m=0.17)	13.7	9.3	6.8	~12.3
1000 (m=0.18)	14.6	9.6	7.0	~4.8

Table 2.7 Estimated flow stress for 10,000 h aged Alloy 617 and Alloy 230

Temperature (^{o}C)	1 Year (MPa)	10 Years (Mpa)	60 Years (MPa)	ASME allowable stress (MPa) [25]
Alloy 230-900 (m=0.20)	13.7	8.6	6.0	~12.3
Alloy 617-1000 (m=0.23)	14.6	8.1	5.3	~4.8
Alloy 230-900 (m=0.21)	10.4	6.4	4.4	~10.2
Alloy 230-1000 (m=0.23)	1.3	0.8	0.51	~2.6

After long-term aging, the strain rate sensitivities show a moderate increase. Table 2.7 summarized the estimated flow stresses for 10,000 h aged Alloy 617 and Alloy 230. The conditions are much more severe for long-term aged materials, especially for Alloy 230. The results suggest that the current ASME allowable stress for both alloys is not applicable for long term and high temperature design.

Chapter 3 – Aging Effect on Alloys

3.1 Overview

Aging studies can provide essential information to predict material behavior for applications at high temperature, and long operation periods. During the aging process, microstructural evolution (e.g. grain growth, precipitates coarsening) will dramatically affect the materials' properties. For nickel-based superalloys, the major feature of microstructural evolution during long-term aging is the precipitation and coarsening process of secondary phases. Since both alloys are candidate materials for IHX and related practical data are not sufficient for engineering application, long-term aging experiments at 900^{o}C and 1000^{o}C were conducted (up to 10,000 h) to evaluate their mechanical and microstructure properties.

3.1.1 Microstructural Characteristics

High temperature aging of metallic materials often causes microstructural evolution, which is mainly characterized by phase transformation, precipitate development, and crystallite growth [25]. Phase transformation will fundamentally change the material properties, which can be evaluated by phase diagram.

The nucleation and growth of second particles is the dominant microstructural feature in the thermal aging process. Solution treatment is required in initial alloying processing, and the alloy only contains a single phase. There are insufficient levels of distribution of the heterogeneous elements (e.g. Cr) at low temperature for major second phase

development. At higher temperature, significant thermal diffusivity of solute leads to second phase particle precipitation at grain boundaries or within grains. This happens over a wide range of temperatures. After the alloy is aged at high temperature, the supersaturated elements begin to diffuse and form clusters. Fine second phase particles nucleate within the grains and at respective grain boundaries. At the same time, the larger particles grow at expense of smaller particles. When the equilibrium condition is achieved, the nucleation process is completed. This process is named as Oswald ripening. The growth of the larger second phase particles at the expense of the smaller ones reduces the total amount of interfacial area between phases in order to decrease the total free energy. This is the driving force of Oswald ripening or carbides coarsening. During heat treatments, four types of particles were found in Alloy 617 and Alloy 230 in previous studies: M_6C, $M_{23}C_6$, Ti (N, C) and $\gamma'(Ni_3Al)$ [19, 29].

M_6C carbides have a complex cubic structures (fcc) and form in a temperature region of 815^{o}C to 980^{o}C. The lattice parameter of M_6C carbides is 1.085-1.175 nm. They tend to be rich in refractory elements (e.g. Fe, Mo, Co, W) depending on material composition. The formation of M_6C carbides requires high Mo or W content in nickel based superalloys (6 to 8 atomic percent). The M_6C carbides in Alloy 617 are rich in Mo and those in Alloy 230 are rich in W. $M_{23}C_6$ carbides are formed in the lower temperature regime of 760^{o}C to 980^{o}C compared to M_6C carbides with moderate to high Cr content. The lattice parameter of $M_{23}C_6$ carbides is 1.150-1.070 nm. The phase also displays a complex cubic structure (fcc) [20]. $M_{23}C_6$ carbides are found to be rich in Cr, the rest of

the composition of M can be made up of different metallic atoms (e.g. Ni, Fe, Mn, Mo, W). [25]

M_6C and $M_{23}C_6$ are the major particles found in the present study. Both types of carbides can impede grain boundary sliding (Zener pining) and increase the rupture strength of materials. On the other hand, they have negative effects on material performance that initiate premature failures by particle decohesion or particle fracture. These particles can withstand temperature up to 1000^{o}C. Related research results on Alloy 617 are presented in Fig 3.1 and Fig 3.2. Transformation and reaction also exist between M_6C and $M_{23}C_6$ according to the following chemical equation:

$$M_6C \underset{M''}{\overset{M'}{\rightleftarrows}} M_{23}C_6 \qquad (3\text{-}1)$$

Where M' and M'' are substitute elements. For Alloy 617, M' is Cr, and M'' is Mo. [25]
Since M_6C and $M_{23}C_6$ are formed during heat treatment and have good thermal stability at high temperature, research on their behavior during long-term aging is essential for IHX applications.

γ'(Ni_3Al) precipitate is an important strengthening phase in nickel based superalloys. It is the third most common feature of the aged materials. Its yield strength increases with temperature up to 800^{o}C [20]. Similarly, the small amount of Ti (N, C) also has an negligible effects on mechanical properties. Ti (N, C) can be detected in Alloy 617, and it is hardly ever found in Alloy 230 due to even lower fraction of Ti. However, both Alloys 617 and 230 are solid solution strengthening alloys (not employing γ' strengthening),

and only very small amounts of γ' were reported in aging studies of Alloy 617 [5]. Also γ' has never been found in both alloys at temperature higher than 900°C.

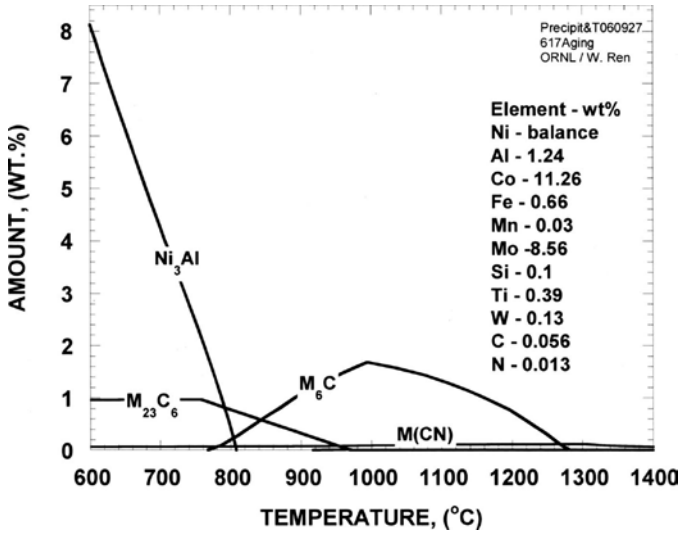

Fig 3.1 Content of Precipitates in Alloy 617calculated by THERMOCALC® (1.24% Al) [29]

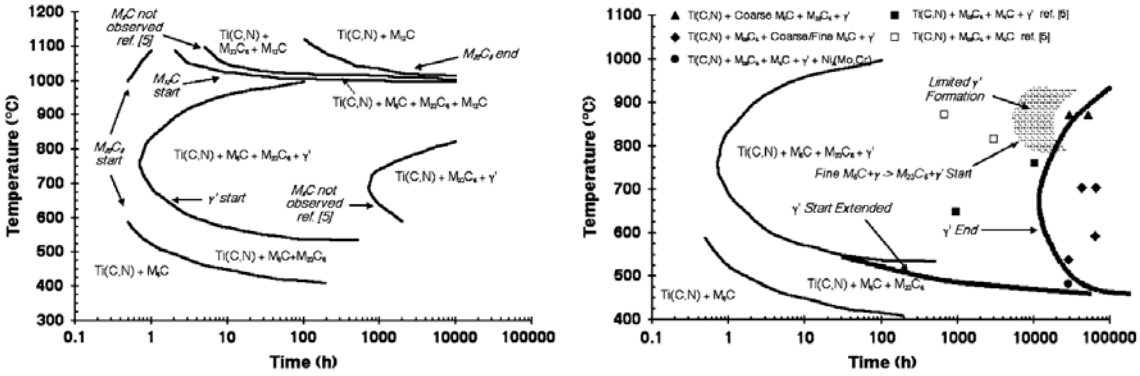

(a) (b)

Fig 3.2 TTT diagram for Alloy 617 (a) constructed based on previous results (b) modification made by Wu et al. [30]

3.1.2 Mechanical Properties

Microstructure development during aging will change the mechanical properties of both alloys. It is important to know that the ability of a metal to plastic deform depends on the mobility of dislocations, and greater mechanical forces are required to continue plastic deformation due to the strengthening methods that impede dislocation motion. Five fundamental strengthening mechanisms contribute to overall strength of alloys: grain boundary hardening τ_{HP} ("HP" denotes Hall-Petch relationship), strain hardening τ_{sh}, dislocation cutting τ_{cut}, dislocation looping τ_{loop}, and solution hardening τ_{sss}. The overall strength τ_{tot} of alloys can be described by equation as [25]

$$\tau_{tot} = \tau_0 + \tau_{HP} + \tau_{sh} + \tau_{sss} + \tau_{loop} + \tau_{cut} \tag{3-2}$$

Where τ_0 denotes intrinsic strength of material

The grain size (or average grain diameter) in polycrystalline materials has a great effect on mechanical properties. Since two adjacent grains have two different orientations and atomic disorder exists within grain boundaries, the dislocation that passes though the grains have to change directions and overcome the resistance from discontinuous slip planes. Therefore, grain boundary strengthening comes from the barrier effect to the movement of glide dislocations. From the work of Petch and Hall, the yield strength of a polycrystalline material can be given by

$$\sigma_{ys} = \sigma_i + k_y d^{-1/2} \tag{3-3}$$

Where, σ_{ys} = yield strength

σ_i = overall resistance of lattice to dislocation movement

k_y = "locking parameter" that measures relative hardening contribution of grain boundaries

d = grain size

Even though much following research indicates that grain boundary-induced dislocation pileups may not be directly related to yield strength described above, a model that consider the grain boundaries as dislocation source by Li [31] still has a similar form:

$$\sigma = \sigma_i + \alpha G b \sqrt{\rho} \tag{3-4}$$

Where, σ = yield strength

σ_i =overall resistance of lattice to dislocation movement, α constant

G= shear modulus, b the Burgers vector, and ρ the average dislocation density.

Note that ρ is inversely proportional to grain size, equations (3-4) and (3-3) are equivalent.

Stain hardening (also known as work hardening or cold working) describes an increase in the number of dislocation-dislocation interaction which reduces dislocation mobility, and sufficient stress has to be applied to continue deform process. Research on strain hardening behavior of single crystals showed three distinct regions in the shear stress strain curve: Stage I (easy glide region), Stage II (linear hardening region), and Stage III (parabolic region) which closely resembles strain stress response of polycrystal form material [32]. Stacking fault energy is important to the onset of Stage III. Stage III would occur sooner with higher stacking fault energy since cross-slip would be activated at a lower stress. Therefore, a low stacking fault energy material requires a larger stress to

combine partial dislocations and cross-slip. The effects of strain hardening may be removed by annealing heat treatment.

Solid solution strengthening is a strengthening mechanism where adding atoms of different elements to base material lattice increases the dislocation flow stress. The reason alloys are stronger than pure metals is that impurity atoms in the solid solution impose lattice strains on the surrounding host atoms. Substitutional solid solution and interstitial solid solution are the two major types of solid solution strengthening. The solid solution elements can generate symmetrical or asymmetrical stress fields: when the stress field is symmetrical, the solute atom interacts with edge dislocation; Otherwise in the asymmetrical stress field instance, the solute atom interacts strongly with both edge and screw dislocations. The magnitude of strengthening caused by asymmetrical stress field is much greater. The strengthening contribution to yield strength can be given by:

$$\tau = \frac{G\varepsilon^{3/2}c^{1/2}}{700} \tag{3-5}$$

Where, τ = stress required for dislocation cutting though

ε= the misfit strain (proportional to difference in lattice parameter of the two phases)

c= the solute concentration (expressed as atomic fraction)

For nickel based alloys, the solid solution often generates symmetrical stress fields [33]. Solid-solution hardening also indirectly decreases the stacking fault energy in the crystal lattice, which enhance the inhibition of dislocation cross slip. [20]

Second phase particles start to nucleate and grow when the solute concentration exceeds the solubility limits. The precipitation of particles in the matrix increases the difficulty of dislocation movement. Two typical strengthening mechanisms are based on dislocation-particle interaction: dislocation cutting and dislocation looping. Some small and highly coherent particles are deformable and dislocation can cut though them under sufficiently high stress. The dislocation cutting mechanism is related to elastic interaction between them:

$$\tau = CG\varepsilon^{3/2}(fr/b)^{1/2} \tag{3-6}$$

Where, τ = stress required for dislocation cutting though

ε= the misfit strain

r = the particle radius

f = the volume fraction of second phase precipitates

G =the shear modulus, and b the Burgers vector.

If the misfit strain (or average particle separation) is large above a critical value, the dislocation cutting mechanism is not applicable, and dislocations will loop around individual particles instead. It requires a larger stress to keep the movement and this dislocation particle interaction is also referred as Orowan looping. The stress that necessary for dislocation looping can be described by:

$$\tau = \frac{Gb}{L-2r} \tag{3-7}$$

Where, τ = stress required for dislocation cutting though

G = the shear modulus

b = the Burgers vector

L = the distance between pinning points

r = the particle radius

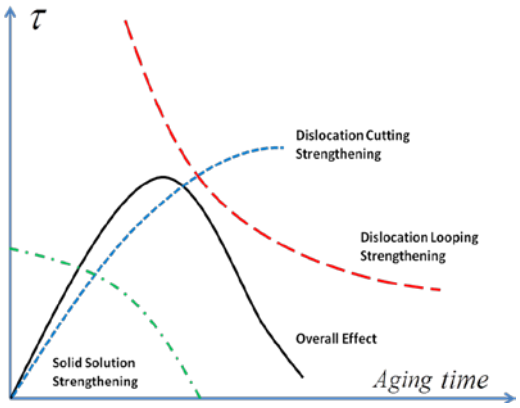

Fig 3.3 Aging effect summary [32]

The combined effect of these complex strengthening mechanisms is responsible for mechanical property changes during the material aging process. In the early stages of the aging process, the precipitation of second phase particles weakens the solid solution strengthening, but it is compensated by enhanced precipitation impeding dislocation movement. This results in an increasing in hardening with time. With further aging, interparticle spacing becomes wider and particle sizes increases, and often the dislocation interactions change from particle cutting to looping. Therefore the alloy strength is weaken with further aging time. The overall aging effect is summarized in the Fig 3.3.

3.2 Microstructure Evolution over Aging Period

3.2.1 Particle Growth

The dominant feature of long-term aged material microstructures is the precipitation, growth and diffusion of second phase particles. Most of the fine precipitates that are found within matrix in the as-received material diffuse and precipitate in the grain

boundaries. Both alloys experienced similar change of carbides: after 900°C aging, the intergranular particles in the bright band-like shape, and coarsening at the expense of fine precipitates within the grain matrix; after 1000°C aging, the intergranular precipitates coalesce to form the bigger dark particles. The coarsening mechanism is revealed by EDS analysis. Fig 3.4 and Fig 3.5 show the EDS spectra of intrinsic particles in Alloys 617 and 230 respectively. Previous research indicates that Cr-rich carbides are $M_{23}C_6$ (dark), Mo-rich and W-rich carbides are M_6C (bright). [25, 30]

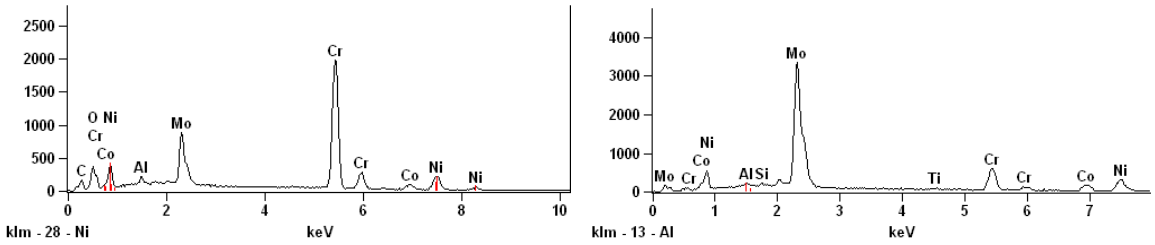

(a) (b)

Fig 3.4 SEM spectra recorded from (a) Cr-rich carbides ($M_{23}C_6$) in Alloy 617 (b) Mo-rich carbides (M_6C) in Alloy 617

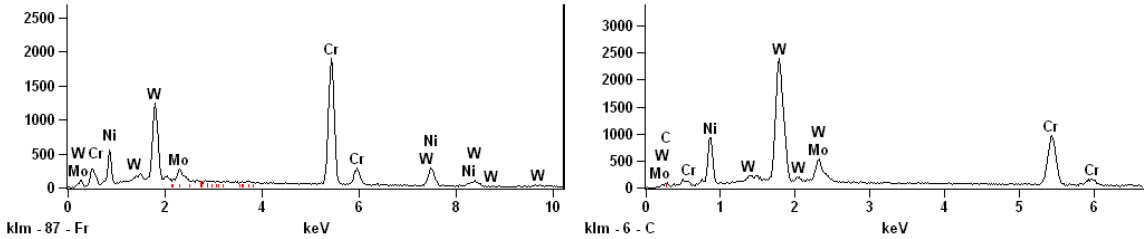

(a) (b)

Fig 3.5 SEM spectra recorded from (a) Cr-rich carbides ($M_{23}C_6$) in Alloy 230 (b) W-rich carbides (M_6C) in Alloy 230

In the as-received alloy 617 specimens, inclusion particles are M_6C, rich in Mo with a bright color. Similar inclusion particles with dark plaques are found in the 900°C long-term aged Alloy 617. These dark plaques are found to be rich in Cr. A comparison of elements concentration was conducted by line scan analysis on inclusion particles. Fig 3.6 shows the counts variation along the specific line and corresponding inclusions.

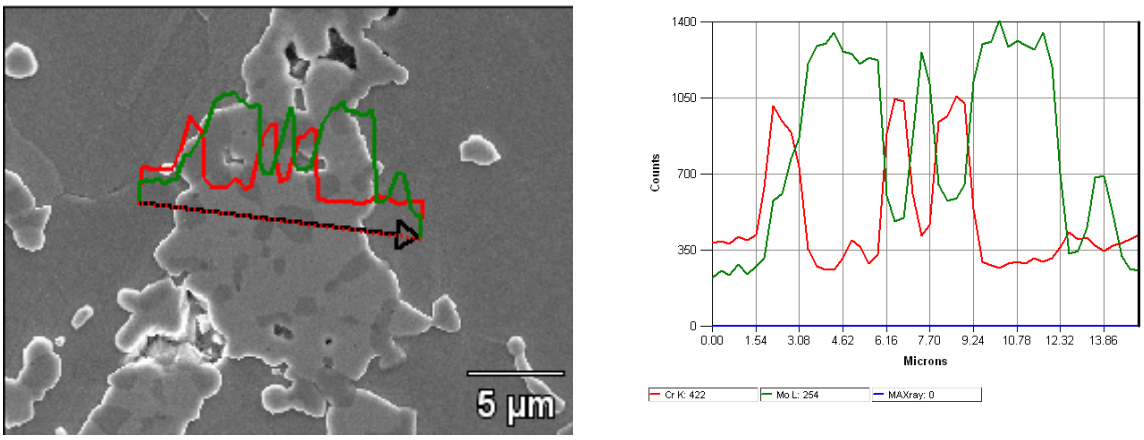

Fig 3.6 EDS line scan result of inclusion particles of 10,000 h aged Alloy 617 at 900°C

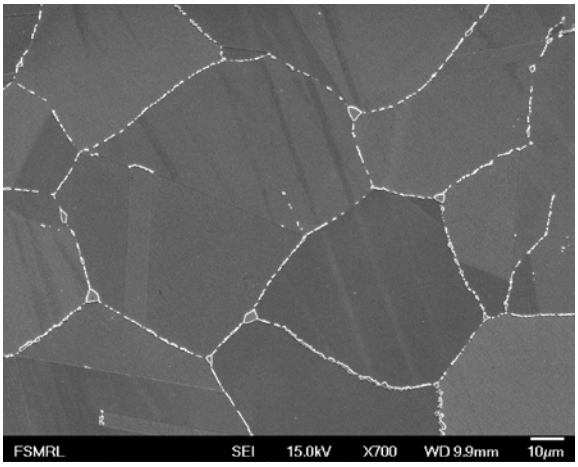

(a)

Fig 3.7 SEM (a) and EDS examination (b) of Mo rich M_6C in Alloy 617 at 900°C

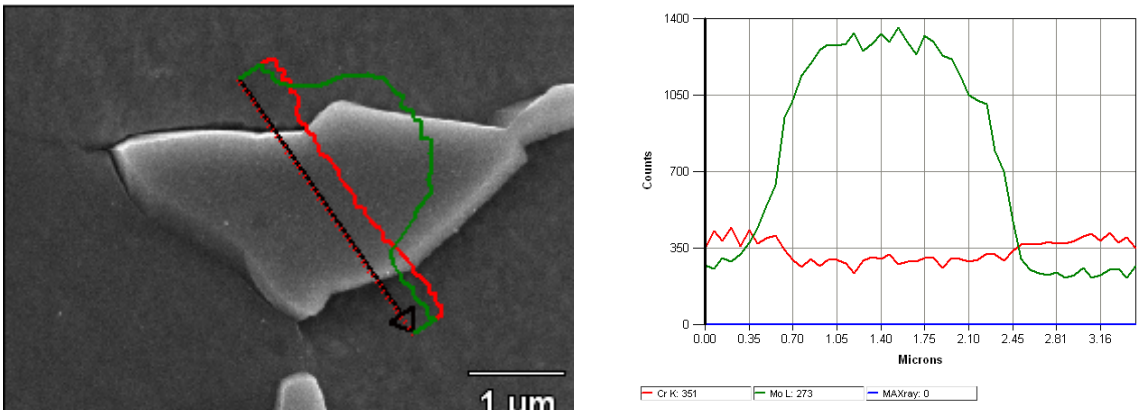

(b)

Fig 3.7 (cont.)

Compared to dark plaques, the bright parts of inclusions have higher intensities in Mo and lower in Cr. Similar examination was conducted on inclusion particles in 1000^{o}C aged Alloy 617. Bright Mo rich particles were seldom observed in the specimens. The big inclusion particles are rich in Cr. Since M_6C has a higher thermal stability than $M_{23}C_6$ at temperature up to 1000^{o}C and Mo/W intensities are high in EDS spectra, phase transformation is unlikely to take place during high temperature aging. The explanation of this phenomenon is that $M_{23}C_6$ carbides diffuse and mixed with M_6C carbides. Due to the higher diffusion coefficient and weight percents, the formation of $M_{23}C_6$ carbides with high Cr concentration is preferable. Compared to W, Mo still has some diffusive ability and Mo rich M_6C coarsening was observed in triple junction point in long term aged Alloy 617 at 900^{o}C. Fig 3.7 shows the EDS spectra and SEM examination of Mo rich M_6C carbides in corresponding Alloys. Similar coarsening phenomena were observed in some W rich M_6C carbides at grain boundaries, and most of carbides are partial Cr rich and partial W rich for long term aged Alloy 230 at 900^{o}C (Fig 3.8). For

both alloys, most intrinsic particles are dark and rich in Cr at higher aging temperature (1000^{o}C)

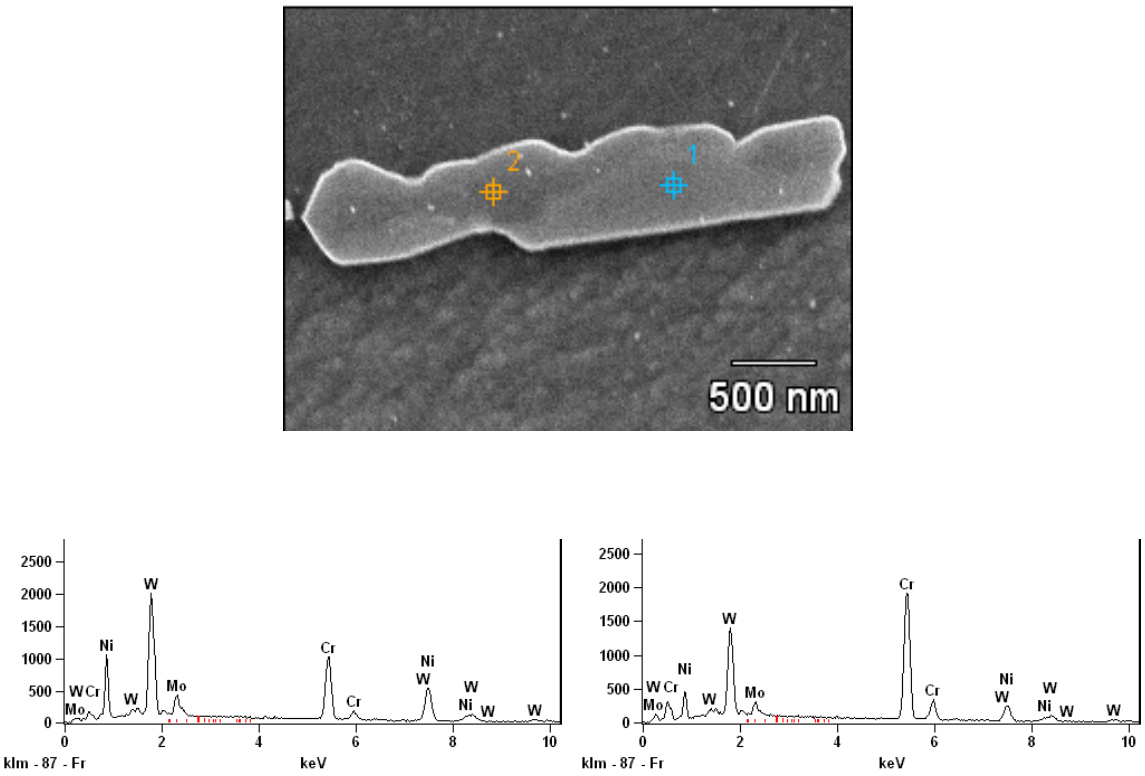

(a) (b)

Fig 3.8 EDS examination of intergranular carbides in long term aged Alloy 230 at 900^{o}C: (a) point 1 (b) point 2

In order to study the kinetics of carbide growth, the coarsening process in grain boundaries was analyzed by measuring particle volume increase. Around 50 intergranular particles were measured from SEM images of 10,000 h aged materials. Particle volume measurement data of as received materials and short-term aged materials (up to 3000 h) were retrieved from Kun Mo's dissertation [25]. The volume was calculated by measuring width and length under the basic assumption that shape is ellipsoidal during long term aging:

$$V(t) = \frac{4}{3} r^2 h \tag{3-8}$$

Where, V = volume of second phase particles

r = radius of ellipsoid particles

h = height of ellipsoid particles

Fig 3.9 shows the measurement of carbides width and length.

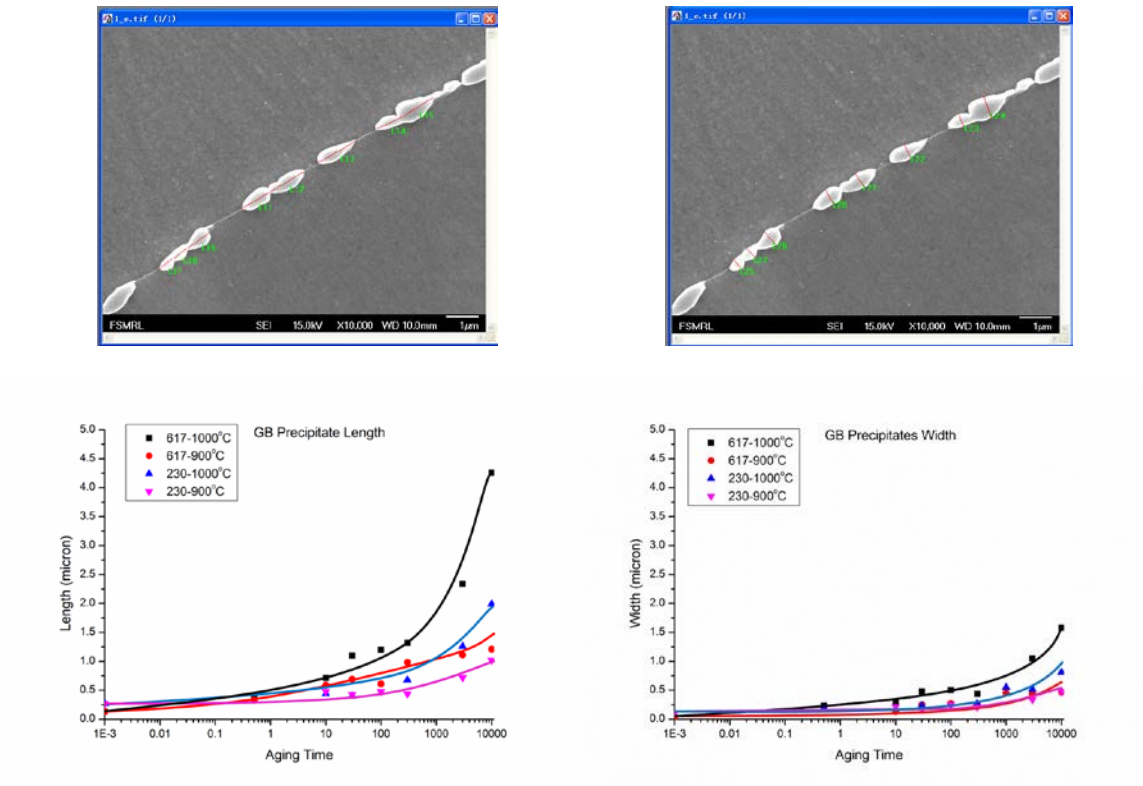

(a) (b)

Fig 3.9 Intergranular Dimension of both alloys: (a) Length (b) Width

Then the volume development for the particle can be fitted by Avrami equation [25]:

$$Y = 1 - \exp(-Kt^n) \tag{3-9}$$

Where, Y = the particle volume fraction, t denotes time, K and n are fitting constant. Y can be expressed as:

$$Y = \frac{V(t)}{V_{mat}} \tag{3-10}$$

Where, V_{mat} is the volume of matured second phase particles. The intergranular particles were assumed fully developed after aging for 10,000 hours and little additional volume will be obtained at longer aging time. Therefore, it is reasonable assume *V (10,000 h)* to be equal to V_{mat}. Fig 3.10 presents fit curves for time dependent intergranular particle volume growth for Alloy 230.

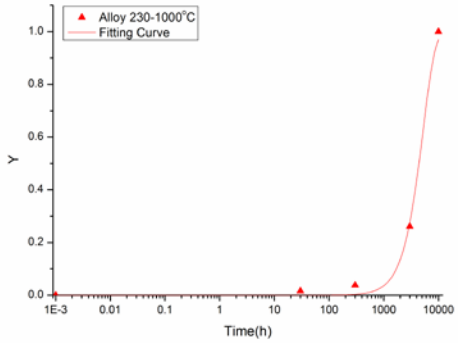

Fig 3.10 Fitting curve and measured data for particle volume in Alloy 230 at 1000°C

Table 3.1 Interpretation of values of n

	n	**Mechanism [34]**
900°C aged Alloy 617	0.65	Thickening of large plates ($n \approx 0.5$)
1000°C aged Alloy 617	2.06	All shapes growing from small dimensions, decreasing nucleation rate ($1.5 < n < 2.5$)
900°C aged Alloy 230	1.59	
1000°C aged Alloy 230	1.99	

Table 3.1 summarizes the possible mechanism of particle development of both alloys at different aging conditions. The "Thickening of large plates" means a dominant

coarsening process, and “All shapes growing from small dimensions, decreasing nucleation rate” indicates a mixed process of particle coarsening and nucleation [34].

3.2.2 Dynamic Recrystallizaion (DRX)

For materials with difference aging hours, the DRX area at specific study temperature is different. Fig 3.11 shows the EBSD results of Alloy 617 of different materials after 900^{o}C tensile test. Longer aging times will result in a higher percentage of DRX area fraction. The DRX in as received alloys can hardly be observed while it is significant in long-term aged specimens. It is also clear that the DRX fractions of 1000^{o}C aged alloys are higher than that of 900^{o}C aged alloys.

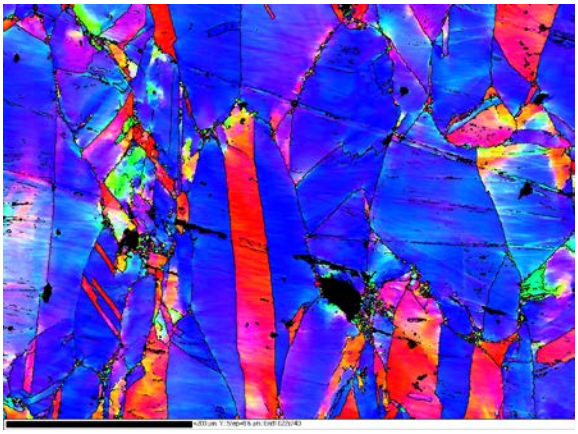

(a)

Fig 3.11 EBSD results of aged Alloy 617 after 900^{o}C tensile test: (a) as received Alloy 617 (b) 900^{o}C aged at 3000 h (c) 1000^{o}C aged at 3000 h (d) 900^{o}C aged at 10,000 h (e) 1000^{o}C aged at 10,000 h

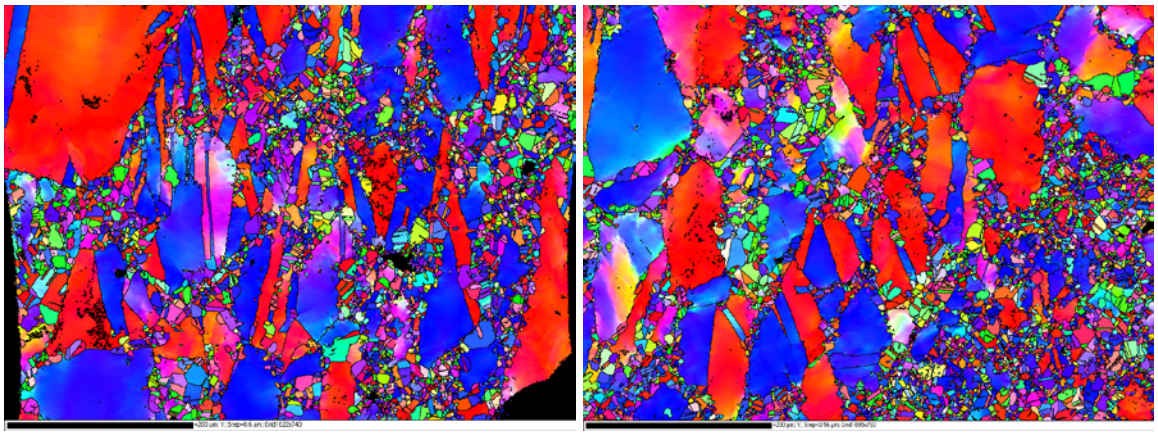

(b) (c)

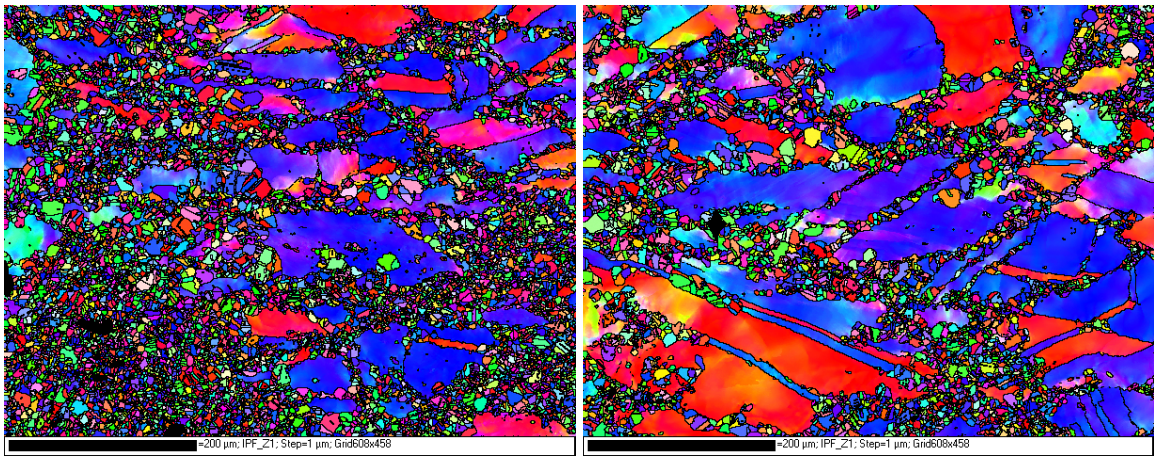

(d) (e)

Fig 3.11 (cont.)

3.3 MECHANICAL PROPERTIES OVER AGING PERIOD

Tensile and hardness tests were conducted for both 10,000 hour aged alloys. The results were summarized along with the data of as-received condition to 3000 hour aging condition by Kun Mo [25] to investigate mechanical properties development as a fuction of the aging time. The tensile tests were performed at a strain rate 10^{-3}/s same

experimental settings given in Chapter 2. The hardness tests were measured using a Wilson® Rockwell® Model 523 hardness tester.

The hardness tests were conducted in all plane directions in order to reflect the overall properties. Then the reported hardness was calculated by averaging the measurement results. The results are presented in Fig 3.12. Both alloys experienced similar trends during aging: the hardness peaks (~94 HRB) were achieved at 10 hours, and then the hardness decreases moderately with aging time. At 900°C, Alloy 230 maintains a longer hardening plateau with only a slight decrease over the aging time. In contrast to 1000°C aging condition, the hardness of both alloys at 900°C aging has a significant increase at 10,000 hours aging time.

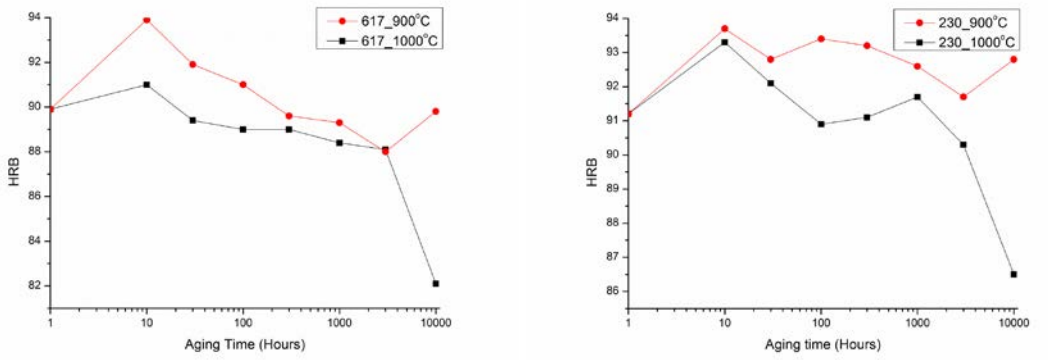

(a) (b)

Fig 3.12 Hardness over aging time: (a) Alloy 617 (b) Alloy 230

Tensile test results over the same aging times are shown in Fig 3.13 and Fig 3.14 for the strength (Y.S.) and ultimate tensile strength (U.T.S.) for Alloy 617 and Alloy 230, respectively. The results, especially the trends in the ultimate tensile strength, agree well with the hardness test results: the materials experienced a short term strengthening and a

long term softening. For the 10,000 hours aged Alloys 617 and 230 at 900°C, the ultimate tensile strength shows a moderate increase. At 900°C, both alloys have higher yield strengths and ultimate tensile strengths for a longer hardening time than those aged at 1000°C, but as aging time increases, the two converge to similar values.

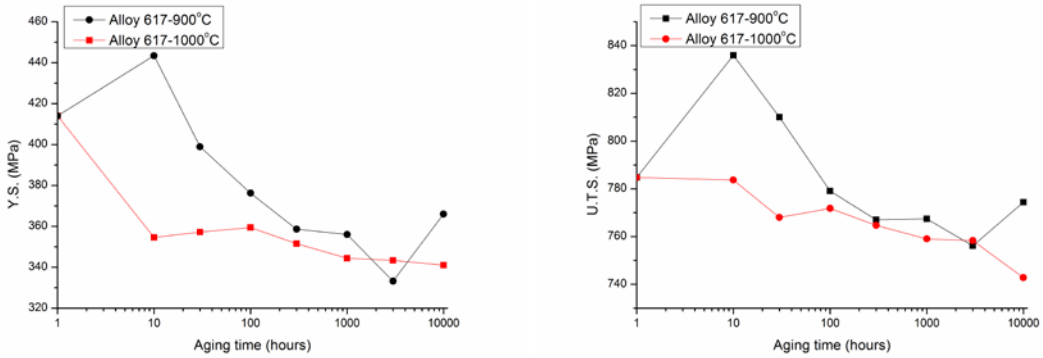

(a) (b)

Fig 3.13 Tensile Properties for Alloy 617: (a) Y.S. (b) U.T.S.

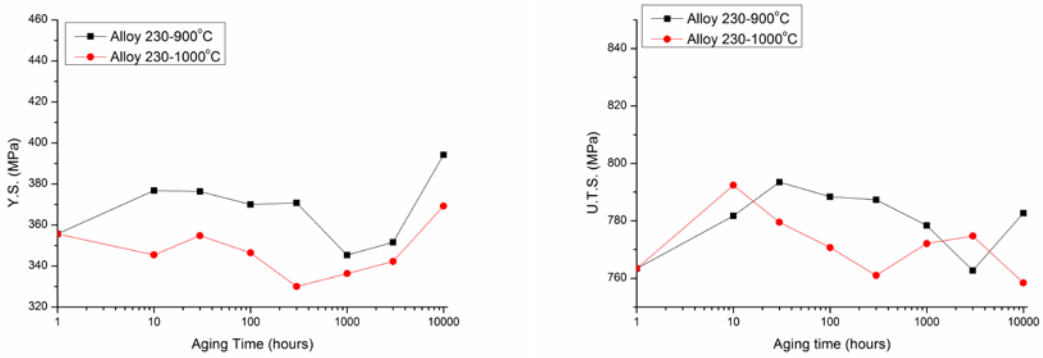

(a) (b)

Fig 3.14 Tensile Properties for Alloy 230: (a) Y.S. (b) U.T.S.

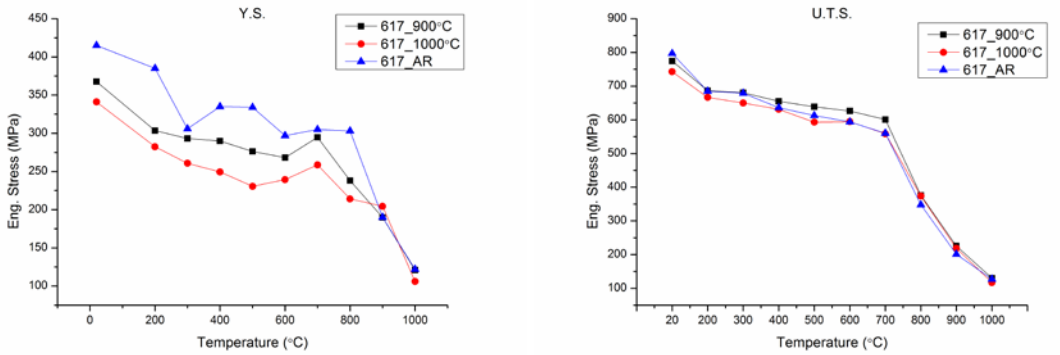

(a) (b)

Fig 3.15 Tensile Properties comparison for Alloy 617

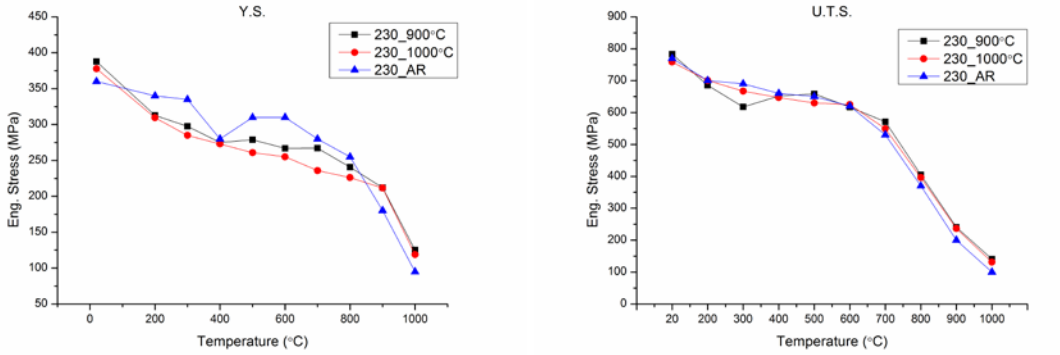

(a) (b)

Fig 3.16 Tensile Properties comparison for Alloy 230

In addition to mechanical properties at room temperature, it is also important to investigate the aging effect on tensile properties at high temperatures, especially in the region of 800^{o}C to 1000^{o}C for IHX application. Fig 3.15 and Fig 3.16 show the comparison of as-received and 10,000 hours aged Alloy 617 and Alloy 230. The yield stress and tensile stress are found to be higher than as-received materials in some regions,

and softening regions are also observed. The Y.S. and U.T.S. changes after 10,000 hours aging can be quantified by:

$$Y.S._{change} = \frac{Y.S.(T, t=0) - Y.S.(T, t=10,000h)}{Y.S.(T, t=0)} \quad (3\text{-}11)$$

$$U.T.S._{change} = \frac{U.T.S.(T, t=0) - U.T.S.(T, t=10,000h)}{U.T.S.(T, t=0)} \quad (3\text{-}12)$$

Where, T is tensile test corresponding temperature, t is the aging time.

The calculation results were summarized in Table 3.2 and Table 3.3 for Alloy 617 and Alloy 230, respectively. The negative values indicate a hardening effect, and the positive values mean a softening effect. Compared to as-received specimens, 900^{o}C aged Alloy 617 shows moderate increase in U.T.S, and both 900^{o}C and 1000^{o}C aged Alloy 230 exhibit significant hardening effects at high temperature regions (900^{o}C and 1000^{o}C).

Table 3.2 Tensile properties comparison (%) of Alloy 617

Temperature (^{o}C)	**Alloy 617 aged at 900^{o}C (Y.S. change)**	**Alloy 617 aged at 1000^{o}C (Y.S. change)**	**Alloy 617 aged at 900^{o}C (U.T.S. change)**	**Alloy 617 aged at 1000^{o}C (U.T.S. change)**
RT	11.4	17.8	2.8	6.8
200	21.1	26.6	-0.2	2.7
300	4.2	14.8	-0.2	4.3
400	13.4	25.5	-3.0	0.7
500	17.3	31.0	-4.2	3.2
600	9.7	19.4	-5.5	-0.1
700	3.3	15.2	-7.3	0.2
800	21.4	29.4	-8.0	-7.4
900	0.2	-7.6	-12.1	-9.0
1000	0.8	13.1	-2.4	7.8

Table 3.3 Tensile properties comparison (%) of Alloy 230

Temperature (^{o}C)	Alloy 230 aged at 900^{o}C (Y.S. change)	Alloy 230 aged at 1000^{o}C (Y.S. change)	Alloy 230 aged at 900^{o}C (U.T.S. change)	Alloy 230 aged at 1000^{o}C (U.T.S. change)
RT	-7.7	-5.0	-1.6	1.5
200	8.0	9.0	2.1	-0.1
300	11.2	14.9	10.5	3.3
400	1.8	2.5	1.2	2.0
500	10.1	15.9	-1.3	3.1
600	13.9	17.7	0.5	-0.1
700	4.6	15.8	-7.8	-3.6
800	5.6	11.3	-9.4	-7.2
900	-17.7	-17.5	-20.3	-18.3
1000	-31.8	-25.1	-40.7	-31.1

3.4 Discussion

The mechanical properties and microstructual characteristics of long term aged Alloy 617 and Alloy 230 were investigated in the previous section. Compared to theoretical analysis of material strength change during aging time (Fig 3.3), two peaks were observed in hardness verses aging time diagrams for 900^{o}C aged alloys (Fig 3.13(b) and Fig 3.14 (b)). Similar phenomena were also found in U.T.S. diagram. As introduced in Section 3.1.2, the strengthening development involves five strengthening mechanisms: grain boundary strengthening, precipitates strengthening (includes particle cutting and particle looping), strain hardening, and solid solution strengthening. According to the microstructure analysis, the grain size and dislocation density do not change significantly during the aging period, then the grain boundary strengthening and strain hardening parts can be

dropped from the strengthening equation. Therefore, the overall strength can be further analyzed based on the solid solution strengthening and precipitates strengthening.

Kun Mo's dissertation reveals the mechanism that generates the fist strength peak during the aging period [25]. During the early stages of aging, both Alloy 617 and Alloy 230 precipitate a large number of fine second phase particles within the matrix, which leads to major precipitate strengthening. However, the precipitation process is accomplished at the expense of other solute elements in the matrix, and it result in a loss of solid solution strengthening. Since precipitate strengthening is more efficient and effective than solid solution strengthening, the former is sufficient to compensate the latter. This short term aging strengthening phenomenon can be observed in the hardness and tensile results. However, with the extended aging times, the volume of intergranular particle continues increase at the expense of the fine matrix precipitates. The spatial space (L) between particles decreases and diminishes the precipitate strengthening (see Eq. 3-7). This process leads to an overall strength decrease and the hardness and tensile results show a long term softening. It is notable that the short-term hardening was not significant for both alloys aged at 1000^{o}C. Since higher diffusion rates of the solute elements is active at 1000^{o}C, the age hardening process is completed quickly, which can be hardly seen in the diagram. For Alloy 230, a longer age hardening period was observed. It results from slower precipitate growth in Alloy 230 compared to Alloy 617. The process is controlled by solute element W which has a lower diffusivity compared to Mo in Alloy 617.

During the age-softening period, another peak was observed for both alloys aged at 900^{o}C. A similar phenomenon was found in Nb-contaning microalloyed steel during aging at 525^{o}C where the second peak resulted from further precipitation of α phase [35]. After carefully examination, no further fine second phase particle nucleation was found in either Alloy 617 or Alloy 230, and theoretically the further precipitation is not likely according to other studies as indicated in Fig 3.2. The previous section shows that the fracture of both alloys at room temperature tensile tests is triggered by intrinsic particle cracking. The grain boundary particles can have an important influence on mechanical properties. The formation of carbide cracks is believed to be associated with slip to twinning location pile-ups [36]. The voids formed by this process join up by coalescence and result in failure. Similar phenomena were also observed in mild steel by Brindley [37], who claimed that the initiation of ductile facture was intitiated by cracking of grain boundary carbides and inclusions. The EDS spectra and corresponding SEM images (Fig 3.17 and Fig 3.18) show the grain boundary particle and inclusion particle crack in the fracture surface.

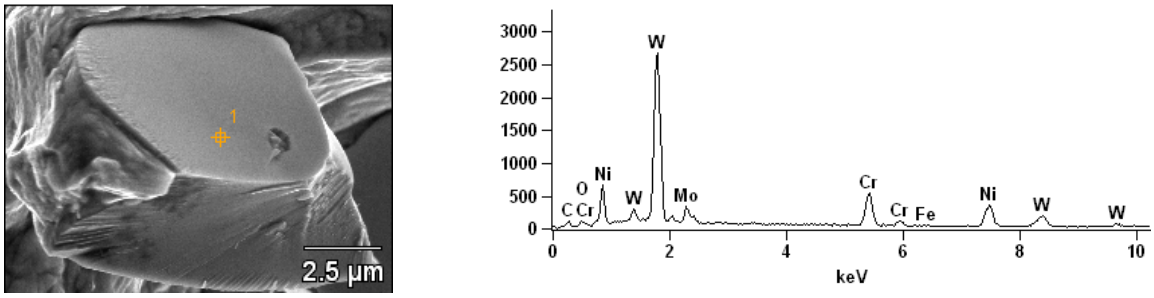

(a)

Fig 3.17 EDS spectra of carbides in fracture surface for Alloy 230 aged at 1000^{o}C:

(a) Inclusion particle (b) Intergranular particle

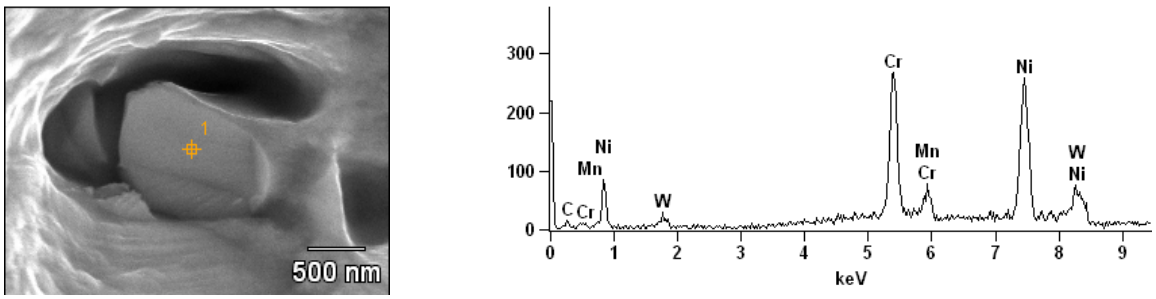

(b)

Fig 3.17 (cont.)

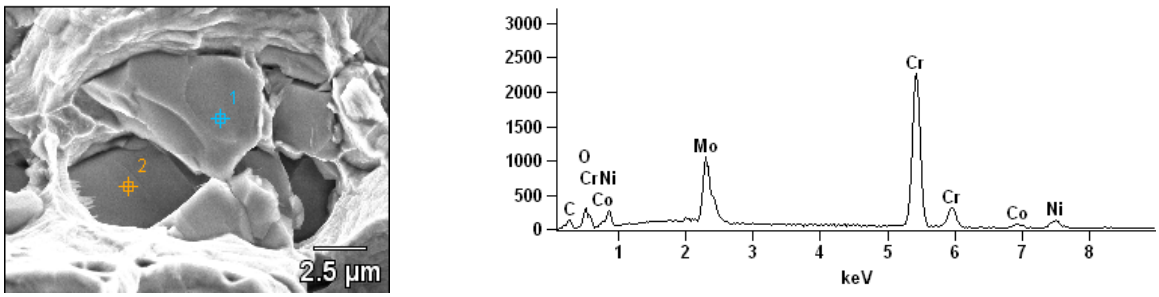

Fig 3.18 EDS spectra of intergranular carbides (point 1 and point 2) in fracture surface for Alloy 617 aged at 1000^{o}C

The strengthening mechanisms result from the effect of impeding dislocation movement. The intergranular particles can be treated as barriers to dislocation. However, the size and shape of these particles have important influence on the dislocation pile-up effect. The effect of small particles to hinder dislocation movement is limited. Fig 3.19 shows the grain boundary particle cracks in Alloy 230 aged at 900^{o}C for 3000 h and 10,000 h, respectively. For 900^{o}C aged Alloy 230, the intergranular particles are relatively small and no cracks can be observed at 3000 h. At 10,000 h, these particles experience coarsening process that small particles coalescence into bigger ones. The bigger particles are elongated along the grain boundaries, and therefore become more efficient barrier for

dislocation movement. More dislocations will be pile-up against these particles so that higher back stress is required for further plastic flow. Second phase particles in matrix are almost disappear so that solid solution strengthening and precipitate strengthening (dislocation looping) are weak. The “strengthening” effect of intergranular particles is sufficient to cover the loss of them. This explains why hardness and U.T.S. are higher at 10,000 h than that at 3000 h.

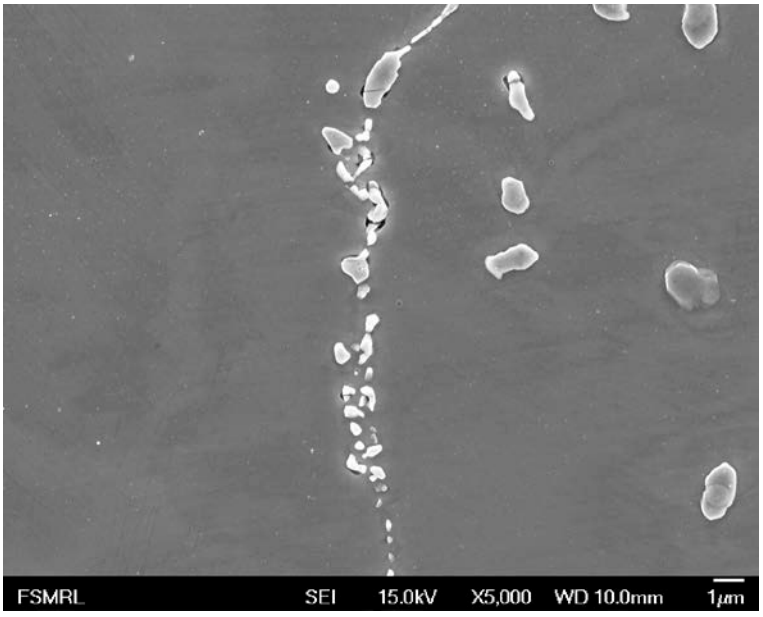

(a)

Fig 3.19 Grain boundary particles crack: (a) 3000 h aged Alloy 230 at 900^{o}C (b) 10,000 h aged Alloy 230 at 900^{o}C

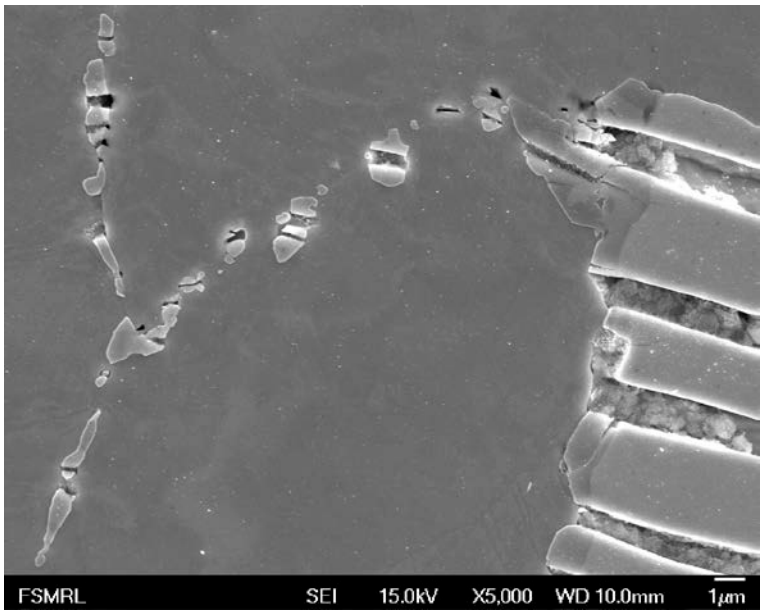

(b)

Fig 3.19 (cont.)

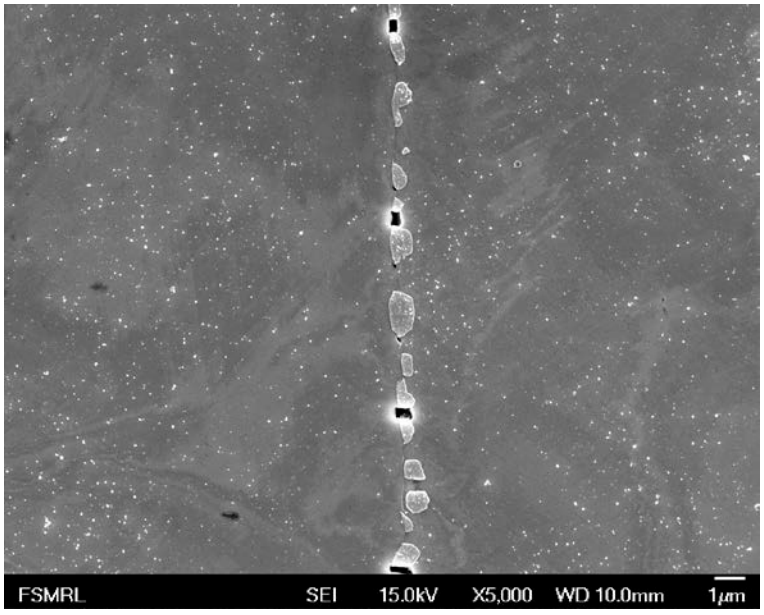

(a)

Fig 3.20 Grain boundary particles crack: (a) 3000 h aged Alloy 230 at 1000^{o}C (b) 10,000 h aged Alloy 230 at 1000^{o}C

(b)

Fig 3.20 (cont.)

A more comprehensive strength change can be observed in the 1000^{o}C aged Alloy 230 from 1000 h to 10,000 h. Fig 3.20 shows grain boundary particles crack for 1000^{o}C at 3000 h and 10,000 h respectively. In this stage (3000 h~10,000 h), grain boundary precipitate coarsening process depletes small particles on the grain boundary rather than those in matrix, since most of fine precipitates were almost completely consumed. Big inclusions also coarsen during long term aging at expense of grain boundary carbides and exhibit higher Cr peak in the EDS spectra (Fig 3.8). Therefore, the volumes of individual intergranular carbide increase, and the carbide spacings are larger with decreasing amunts of carbides. Therefore, the number of effective barrier carbides decreased. This leads to a strength decrease of the alloys at 10,000 h when compared to 3000 h. The second hardness peak was observed in the 900^{o}C aged and 1000^{o}C aged Alloy 230 and 900^{o}C

aged Alloy 617, but not in 1000^{o}C aged Alloy 617. This may be result from different particle development mechanisms in Alloy 617 (see Table 3.1)

Another change that takes place during long term aging is the change in area fraction of DRX. The change is summarized in Table 3.3 for Alloy 617 at 900^{o}C tensile tests. Since a critical dislocation density is essential for the initiation of DRX, the local high dislocation density can be achieved by large deformation (e.g. tensile tests). The preferred site for DRX nucleation is high dislocation density area (e.g. grain boundaries and inclusion rich areas) in both alloys. Tian et al. [37] studied DRX in hot deformed Nimonic 80a alloys. Small coherent carbides within the grains significantly modified the distribution of dislocations during hot deformation by dislocation-particle interaction, and therefore influenced the DRX process. In long-term aged Alloys 617 and 230, since the number and volume of inclusion particles will not change during aging process, the redistribution and coarsening of carbides are responsible for those changes in both alloys. The as-received Alloy 617 is mainly hardened by precipitation strengthening. These small precipitates act as obstacles to dislocation movement, which makes the distribution of dislocations more homogeneous. This reduces the possibility of local high dislocation densities. Compared to long term aged specimens, the DRX process in as-received specimens is not significant. In contrast, during the period of high temperature aging, the fine precipitates in matrix are dissolved and diffuse to the grain boundaries. Dislocations move easily to grain boundaries in absence of those obstacles. Besides, the intergranular particles also form effective barriers to dislocation pile-ups as DRX nucleation sites. For these reasons, DRX in long-term aged specimens is active whereas it is not observed in

starting materials. It is clear from the table that 10,000 h aged specimens contain the largest DRX area fraction. The DRX area factions in Alloy 230 with different aging times but at the same temperature have only slight different (19% for 900^{o}C and 20.3% for 1000^{o}C) due to the appearance of large inclusion, which makes the contribution from grain boundary particles relatively small.

Table 3.4 Area fraction of dynamic recrystallization of Alloy617 at 900^{o}C tensile test

Aging temperature	**As received (%)**	**3000 h aged (%)**	**10,000 aged (%)**
900^{o}C	0.782	22.5	55.9
1000^{o}C	0.782	24.7	35.9

The DRX process has an important effect on mechanical properties. The fracture initiation mechanisms during hot working are summarized in Gandhi's work [38]. The three strain rate dependent mechanisms are ductile cavity initiation, wedge crack initiation and creep cavity initiation. When an alloy is deformed at high strain rates, the ductility is low and the fracture results from cavity initiation around hard second phase particles. The mechanism is called ductile cavity initiation. At medium strain rates, grain boundary sliding takes place. If the sliding displacement is not accommodated, wedge type cracks can initiate at grain triple points. When the strain rate is much lower strain rates, the wedge crack mechanism is replaced by creep cavitation. In this case, round cavities are initiated on grain boundaries normal to the maximum principle stress direction.

Ductile cavity initiation is usually observed in low temperature tensile specimens. At elevated temperatures, the local stress around hard particles can be relaxed by diffusion and power law creep processes. A critical strain rate is required since lower strain rate does not generate sufficient stress concentration to compensate relaxation effects. The critical strain rate $\dot{\varepsilon}_d$ is given by:

$$\dot{\varepsilon}_d = \frac{118(1-\upsilon)(1-2\upsilon+\frac{2}{\pi})}{(\frac{5}{6}-\upsilon)^2}\frac{G\Omega}{kT}\frac{f_\upsilon D_b \delta}{p^3} \tag{3-13}$$

Where, G = Shear modulus

v= Poisson's ratio

D = the boundary diffusion coefficient

δ = boundary thickness

f_v= volume fraction of inclusions or hard particles

p= the particle size

k = the Boltzmann constant

T = Temperature

Hot working maps provide useful information on fracture mechanisms change for specimens at different aging time. Fig 3.21 shows a "safe hot working zone" for pure nickel [38]. The arrows in the figure show the boundary movement during hot working. The driving force of the boundaries movement comes from DRX. The ductile cavity initiation boundary moves upward because of the relaxation of stress concentration around these second phase particles. The wedge crack initiation boundary movement results from grain refinement by DRX. The region between these boundaries is the adiabatic heating and oxidation region. The main fracture mechanism in this region is

found to be round cavity formation within grains. The rapid DRX process will prevent the cavities from growing and linking with each other.

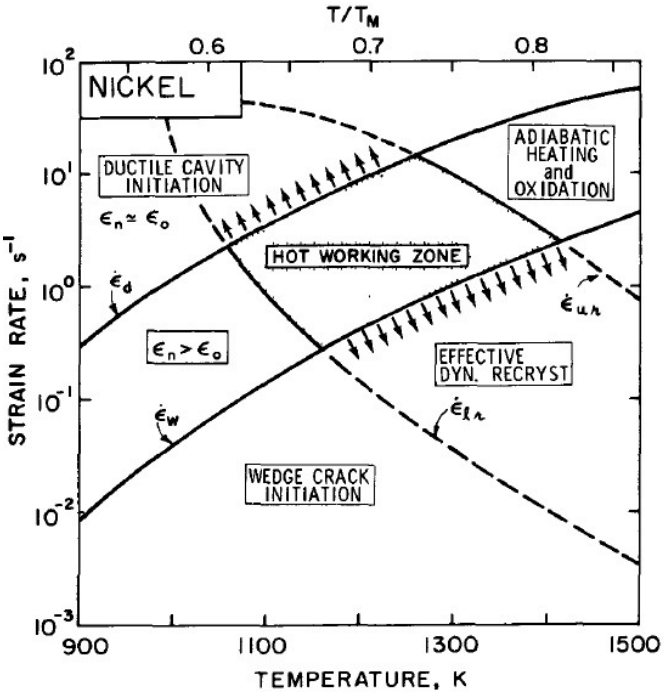

Fig 3.21 Safe hot working zone for nickel [38]

The fracture mechanism change in Alloy 617 and Alloy 230 can be interpreted in a similar way. Fig 3.22 shows the fracture mechanisms for as-received and 10,000 h aged Alloy 617 at 1000°C. It is clear that the crack mechanism in as-received Alloy 617 is wedge-type cracks in triple-point junctions. In contrast, the fracture initiation in 10,000 h aged Alloy 617 shows round cavities within grains and at grain boundary particles. For long term aged Alloy 617, the DRX process is active, and thus the area representing wedge crack initiation in hot work map will shrink. The fracture mechanism will move into the adiabatic heating region. DRX also suppresses fracture initiation by isolating the voids, and therefore preventing cracks from growing and linking to each other. Cracks in Alloy 230 are shown in Fig 3.21. The average particle size of Alloy 230 is much larger

than Alloy 617 due to the appearance of big inclusions. According to Eq. 3-12, the critical strain rate $\dot{\varepsilon}_d$ is inversely proportional to the cube of particle size *p*. Therefore, the critical strain rate $\dot{\varepsilon}_d$ is lower and fracture mechanism is close to the ductile cavity initiation region.

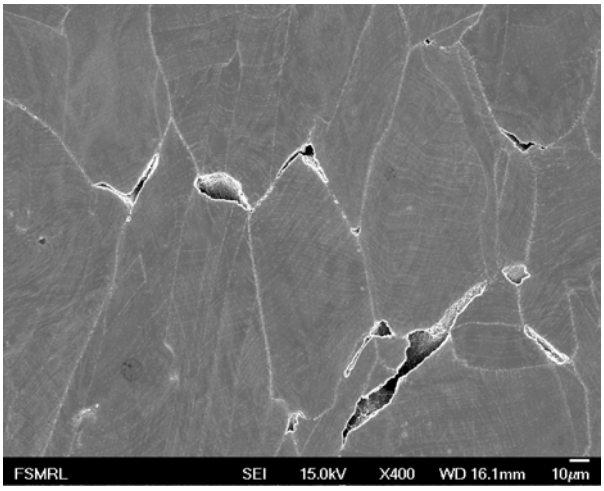

(a)

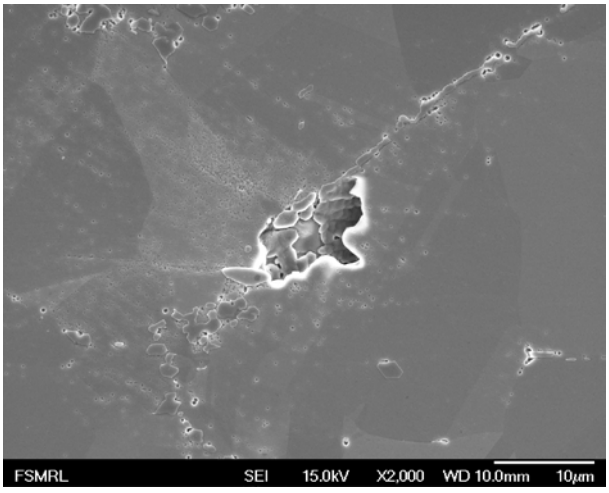

(b)

Fig 3.22 Fracture mechanisms of Alloy617 at 900^{o}C: (a) as-received (b) 10,000 h aged

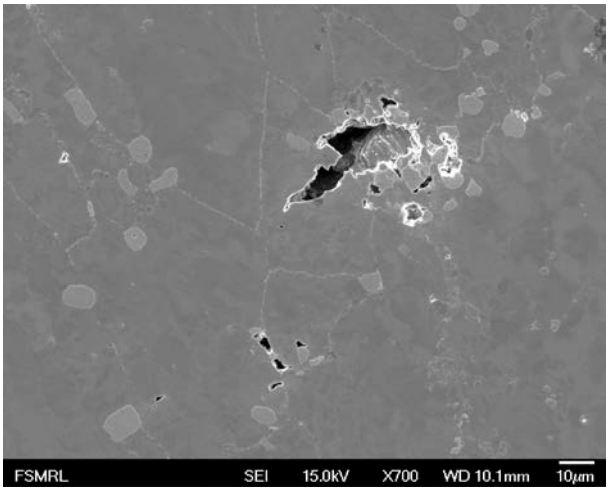

Fig 3.23 Cracks in Alloy 230 at 900^{o}C

Since fracture initiation of both alloys resulted from grain boundary sliding, the coarsening of intergranular particle contributes to tensile properties strengthening at high temperature. These particles can slow down sliding rates and bigger particles are found to be more efficient than small particles with same volume fraction [39]. Higher stresses are required to keep constant strain rate. Therefore, the combined effect of void isolation by DRX and intergranular particle pinning are very likely to contribute to tensile properties improvement at high temperature.

Chapter 4 – Conclusions

Material research is essential for the development of the Very High Temperature Reactor (VHTR). Long term operation (~60 years) at high temperature (760~950^{o}C) poses a great challenge for the candidate materials Alloy 617 and Alloy 230. Long term aging studies on these materials are critical for the design and operation of the VHTR. The research work presented in this thesis mainly evaluates mechanical properties and microstructural features of long-term aged (10,000 h) Alloy 617 and Alloy 230 at two different aging temperatures (900^{o}C and 1000^{o}C). Tensile tests and hardness tests were conducted, and the tested specimens were further analyzed by EDS coupled SEM and EBSD techniques. The experimental results and microstructure characterization lead to the following conclusions:

1. Microstructure Overview:
    a) 10,000 h aged Alloy 617/Alloy 230 at 900^{o}C: significant intergranular carbides coarsening was observed. Intergranular carbides are elongated along grain boundaries with small distance between each other. Most intergranular carbides were Cr-rich, and Cr-rich dark plaques were also observed in Mo-rich (Alloy 617) / W-rich (Alloy 230) inclusions. No phase changes are expected and these plaques result from Cr-rich carbide precipitation.
    b) 10,000 h aged Alloy 617/Alloy 230 at 1000^{o}C: significant intergranular carbides coarsening were observed. The sizes and space between them are larger than for the 900^{o}C aged specimens. Most interguanular and inclusion carbides were Cr-rich, which indicates higher Cr diffusion and precipitate rate at this temperature.

2. Mechanical Properties: For 10,000 h aged specimens, little changes in strain rate sensitivities and Portevin-LeChatelier effects were observed compared to as-received materials. For 900^{o}C, aged Alloy 617 and Alloy 230, the hardness and tensile properties are higher than those of 3000h aged alloys at room temperature. In contrast, 1000^{o}C aged specimens for 10,000 h show worse properties than 3000 h aged specimens. At high temperature, both alloys (especially Alloy 230) exhibit better tensile properties than as-received specimens.

3. Aging effect on mechanical properties:
   a) Room temperature: the mechanical properties changes are related to grain and intergranular particle sizes and distributions. From SEM images of tested specimens, the fracture initiation mechanism is second phase particle cracking. For 10,000 h aged alloys at 900^{o}C, the band-like shape and small intervals make intergranular particles more effective barriers for dislocation movement than those of 3000 h aged alloy; In contrast, the spacing increase in intergranular carbides in the 10,000 h aged alloys at 1000^{o}C results in a decrease of numbers of efficient barriers, which is insufficient to compensate for the precipitate strengthening loss. Therefore, the measured mechanical properties deteriorated.
   b) High temperature (900^{o}C~1000^{o}C): Fine precipitates in matrix act as obstacles to dislocation movement that result in a more homogeneous dislocation distribution. After 10,000 h aging, most precipitates in the matrix have dissolved. This increases the possibility of high local dislocation densities which, in turn,

enhances the dynamic recrystallization (DRX) process. The large area fraction of DRX suppresses fracture initiation by isolating voids and preventing crack growing. This process and large intergranular particles prevent wedge crack initiation and also impedes grain sliding. Due to the presence of many large inclusions in Alloy 230, the critical stain rate for ductile cavity initiation is lower than for Alloy 617 and that these particles still can effectively hinder dislocation movement at high temperature. Intergranular particles coarsening also will effectively slow down the grain boundary sliding rate. Cavity isolation by DRX and particle blocking grain boundary sliding are likely reasons for mechanical properties improvement at higher temperature for long term aged alloys.

List of References

[1] *Nuclear Power in the World Today*, http://www.world-nuclear.org/info/inf01.html, [referred March. 2012]

[2] GEN IV International Forum, *GIF R&D Outlook for Generation IV Nuclear Energy Systems*, August 21, 2009

[3] *Preparing Today for Tomorrow's Energy Needs*, http://www.gen-4.org/, [referred March. 2012]

[4] U.S. DOE Nuclear Energy Research Advisory Committee and Generation IV international Forum, "A Technology Roadmap for Generation IV Nuclear Energy Systems," December, 2009

[5] W. Ren, R. Swindeman, "A Review on Current Statues of Alloy 617 and Alloy 230 for Gen IV Nuclear Reactor Internals and Heat Exchangers," *Journal of Pressure Vessel Technology, Transactions of ASME*, vol. 131, no. 4, pp. 0440021-04400215, 1998

[6] J. K. Wright, R. N. Wright (INL), T.-L. Sham (ORNL) "Next Generation Nuclear Plant Steam Generator and Intermediate Heat Exchanger Materials Research and Development Plan," *Idaho National Laboratory Plan*, Project No. 23747, Document ID PLN-2804, 2010

[7] Special Metals Corporation, Inc. "INCONEL alloy 617," Publication No. SMC-029, 2005

[8] Ren W., Swindeman R. W., "Development of A Controlled Material Specification for Alloy 617 for Nuclear Applications," *Oak Ridge national Laboratory*, 2005

[9] HAYNES International, Inc. "HAYNES 230 Alloy," Publication No. H-3060D, 2009

[10] G. Baccaglini, S. Ball, T. Burchell, B. Corwin, T. Fewell, M. LaBar, P. MacDonald, P. Rittenhouse, E. Shaber, F. Southworth, R. Vollman, "Very High Temperature Reactor (VHTR), Survey of Materials Research and Development Needs to Support Early Deployment," *Generation IV nuclear energy systems*, INEEL/EXT-03-00141, 2003

[11] Wright N. R., "Summary of Studies of Aging and Environmental Effects on Inconel 617 and Haynes 230," *Idaho National Laboratory*, INL/EXT-06-11750, 2006

[12] W. L. Markins, W. J. Hosier, "Microstructure and Phase Stability of INCONEL Alloy 617," *Metall. Trans.*, vol. 5, pp. 2579-2590, 1974

[13] G. F. Kimball, G. Y. Lai, G. H. Reynolds, "Effects of Thermal Aging on Microstructural and Mechanical Properties of a Commercial Ni-Cr-Co-Mo Alloy (Inconel 617)," *Metall. Trans. A*, vol. 7A, pp. 1951-1952, 1976

[14] H. Kirchhofer, F. Schubert, H. Nickel, "Precipitation Behavior of Ni-Cr-22Fe-18Mo (HASTELLOY X) and Ni-Cr-2Co-12Mo (INCONEL 617) after Isothermal Aging," *Nuclear Technology.* vol. 66, pp. 139-148, 1984

[15] U. Bruch, D. Schumacher, P. Ennis, E. Heesen, "Tensile and Impact Properties of Candidate Alloys for High-Temperature Gas-Cooled Reactor Applications," *Nuclear Technology.* vol. 66, pp. 357-362, 1984

[16] D. Kim, I. Sah, D. Kim, W. S. Ryu, C. Jang, "High Temperature Oxidation Behavior of Alloy 617 and Haynes 230 in Impurity-Controlled Helium Environments," *Oxidation of Metals.* vol. 75, no. 1-2, pp. 103-119, 2011

[17] S. Chatterjee, A. K. Roy, "Mechanism of Creep Deformation of Alloy 230 Based on Microstructral Analysis," *Materials Science and Engineering A.* vol. 527, no. 29-30, pp. 7893-7900, 2010

[18] S. Gosse, T. Alpettaz, S. Chatain, C. Gueneau, "Chromium Activity Measurements in Nickel Based Alloys for Very High Temperature Reactors: Inconel 617, Haynes 230, and Model Alloys," *Journal of Engineering for Gas Turbines and Power.* vol. 131, no. 6, 2009

[19] K. Mo, G. Lovicu, H. Tung, X. Chen, J. F. Stubbins, "High Temperature Aging and Corrosion Study on Alloy 617 and Alloy 230," *Journal of Engineering of Gas Turbines and Power.* vol. 133, no. 5, 2011

[20] B. Geddes, H. Leon, X. Huang, (2010). *Superalloys: Alloying and Performance.* Materials Park, Ohio: ASM International.

[21] W. L. Mankins, J. C. Hosier, T. H. Bassford, "Microstructure and Phase Stability of INCONLE 617," *Metallurgical Transactions.* vol. 5, pp. 2579-2590, 2009

[22] W. R. Corwin, T. D. Burchell, C. E. Duty, Y. Katoh, J. W. Klett, T. E. McGreevy, R. K. Nanstad, W. Ren, P. L. Rittenhouse, L. L. Snead, R. W. Swindeman, D. F. Wilson, "Next Generation Nuclear Plant Materials Research and Development Program Plan," (Revision 3), INL/EXT-06-11701, 2006

[23] R. Raj, "Development of Processing Map for Use in Warm-Forming and Hot-forming Process," *Metallurgical Transactions A,* vol. 12A, pp. 1089-1097, 1981

[24] G. E. Dieter, (1988). *Mechanical Metallurgy (3rd ed.),* Columbus, Ohio: McGraw-Hill.

[25] K. Mo, *Microstructural Evolution and Mechanical Behavior In Nickel Based Alloys for Very high Temperature Reactor.* Dissertation, University of Illinois at Urbana-Champaign, 2011

[26] M. S. A. Karunaratne, R.C. Reed, "Interdiffusion of the platinum-group metals in nickel at elevated temperatures," *Acta Materialia,* vol. 51, pp. 2905-2919, 2003

[27] F. Montheillet, J. -P. Thomas, "Dynamic Recrystallization of Low Stacking Fault Energy Metals," *Metallic Materials with High Structural Efficiency,* pp. 357-368, 2004

[28] F. Montheillet, "Moving Grain Boundaries during Hot Deformation of Metals: Dynamic Recrystallization," *Moving Interfaces in Crystalline Solids,* pp. 203-256, 2004

[29] W. Ren, R. W. Swindeman, "A Review Paper on Aging Effects in Alloy 617 for Gen IV Nuclear Reactor Application," *Journal of Pressure Vessel Technology,* vol. 131, 2009

[30] Q. Wu, H. Song, R. W. Swindman, J. P. Shingledecker, V. K. Vasudevan, "Microstructure of Long-Term Aged IN617 Ni-Base Superalloy," *Metallurgical and Materials Transactions A,* vol. 39A, pp. 2569-2585, 2008

[31] J. C. M. Li, "Petch Relation and Grain Boundary Sources," *Transactions of the Metallurgical Society of AIME,* vol. 227, pp. 239-247, 1963

[32] R. W. Hertzberg, (1996). *Deformation and Fracture Mechanics of Engineerign Materials (4th ed.),* Hoboken, New Jersey: John Wiley & Sons

[33] M. A. Meyer, K. K. Chawla, (2008). *Mechanical Behavior of Materials,* New York: Cambridge University Press

[34] J. W. Christian, (1975). *The Theory of Transformations in Metal and Alloys – Part I: Equilibrium and General Kinetic Theory.* Pergamon Press.

[35] S. Q. Yuan, H.B. Wu, C.J. Shang, X.L. He, "Formation of two hardening peaks in Nb-containing microalloyed steel during aging," *Transaction of Material and Heat Treatment,* vol. 26, pp. 69-73, 2005

[36] T. C. Lindley, G. Oates, C.E. Richards, "A Critical Appraisal of Carbide Cracking Mechanisms in Ferride/Carbide Aggregates," *Acta Metallurgica,* vol. 18, pp. 1127-1136, 1970

[37] B. Tian, C. Lind, O. Paris, "Influence of $Cr_{23}C_6$ carbides on dynamic recrystallization in hot deformed Nimonic 80a alloys," *Materials and Engineering,* vol. A358, pp. 44-51, 2003

[38] C. Gandhi, "On Fracture Initiation Mechanisms and Dynamic Recrystallization during Hot Deformation of Pure Nickel," *Metallurgical Transactions A,* vol. 13A, pp. 1233-1238, 1982

[39] R. Raj, M. F. Ashby, “On Grain Boundary Sliding and Diffusional Creep,” *Metallurgical Transactions,* vol. 2, pp. 1113-1127, 1971